*J. Fluid Mech.* (2002), *vol.* 458, *pp.* 35–73.  
DOI: 10.1017/S0022112001007650 Printed in the United Kingdom

# Stability of thermocapillary flows in non-cylindrical liquid bridges

By CH. NIENHÜSER AND H. C. KUHLMANN
ZARM, Universität Bremen, 28359 Bremen, Germany

(Received 15 March 2001 and in revised form 16 October 2001)

The thermocapillary flow in liquid bridges is investigated numerically. In the limit of large mean surface tension the free-surface shape is independent of the flow and temperature fields and depends only on the volume of liquid and the hydrostatic pressure difference. When gravity acts parallel to the axis of the liquid bridge the shape is axisymmetric. A differential heating of the bounding circular disks then causes a steady two-dimensional thermocapillary flow which is calculated by a finite-difference method on body-fitted coordinates. The linear-stability problem for the basic flow is solved using azimuthal normal modes computed with the same discretization method. The dependence of the critical Reynolds number on the volume fraction, gravity level, Prandtl number, and aspect ratio is explained by analysing the energy budgets of the neutral modes. For small Prandtl numbers ($Pr = 0.02$) the critical Reynolds number exhibits a smooth minimum near volume fractions which approximately correspond to the volume of a cylindrical bridge. When the Prandtl number is large ($Pr = 4$) the intersection of two neutral curves results in a sharp peak of the critical Reynolds number. Since the instabilities for low and high Prandtl numbers are markedly different, the influence of gravity leads to a distinctly different behaviour. While the hydrostatic shape of the bridge is the most important effect of gravity on the critical point for low-Prandtl-number flows, buoyancy is the dominating factor for the stability of the flow in a gravity field when the Prandtl number is high.

## 1. Introduction

Thermocapillary flows are important in many technical processes involving non-isothermal fluid interfaces. Such flows are driven by an imbalance of the tangential stress on the interface caused by the temperature-dependence of the surface tension (Scriven & Sternling 1960; Levich & Krylov 1969). The thermocapillary flow is of particular importance in the float-zone crystal-growth technique where it drives significant fluid motion. Since an oscillatory melt flow in these systems results in undesired concentration variations in the grown crystal (Bohm, Lüdge & Schröder 1994), model systems have been studied quite extensively in order to gain insight into the physical processes that determine the onset of melt-flow oscillations. Most important among the models of the float-zone process is the so-called *half-zone* model. In this system adhesion and surface tension hold a finite volume of liquid in the gap between two concentric rigid disks which are kept at different temperatures (Kuhlmann 1999).

The presence of a dynamic liquid–gas interface is one of the major difficulties for a numerical treatment. Therefore, several simplifying assumptions have frequently been made. When the volume of the liquid bridge is very small, for instance, surface

tension forces dominate and the liquid takes a nearly cylindrical shape. The linear stability of the axisymmetric steady toroidal flow in cylindrical half-zones has been considered by Neitzel *et al.* (1993) and Wanschura *et al.* (1995). The analysis of Wanschura *et al.* (1995) provides explanations for the physical instability mechanisms and yields a satisfactory quantitative comparison with the available experimental data for moderately large Prandtl numbers (see e.g. Velten, Schwabe & Scharmann 1991). They accurately calculated the critical Reynolds numbers $Re_c$ characterizing the onset of three-dimensional flow. For small Prandtl numbers ($Pr \ll 1$) typical for crystal-growth applications they found the first instability of the axisymmetric flow to be three-dimensional and stationary. It is caused by inertia effects. For liquids with Prandtl numbers $Pr \gtrsim 1$, which applies to the commonly used transparent model fluids, the first linear instability is oscillatory and the instability is analogous to the hydrothermal-wave instability in plane layers, first discussed by Smith & Davis (1983). Apart from the Prandtl-number dependence, Wanschura *et al.* (1995) found that the critical Reynolds number and the azimuthal wavenumber of the critical mode also depend on the aspect ratio $\Gamma$ (height/radius) of the half-zone.

For a given radius and separation of the heated disks, the shape of the liquid bridge is determined by the volume of liquid. Non-cylindrical interfaces may also arise due to hydrostatic pressure effects, if the length scale is sufficiently large. Experimental evidence (Hu *et al.* 1994; Masud, Kamotani & Ostrach 1997; Sakurai & Hirata 1998) suggests that the critical conditions for the onset of oscillatory flows in high-Prandtl-number liquid bridges depends very strongly on the interface shape. For liquid volumes roughly corresponding to a cylindrical interface the critical Reynolds number has a peaked maximum indicating a very stable flow. A theoretical explanation of this behaviour is still lacking.

Only a few numerical investigations have addressed the stability of the flow in non-cylindrical liquid bridges. Shevtsova & Legros (1998) simulated two-dimensional buoyant–thermocapillary flow to determine the onset of the time-dependence in a half-zone with $Pr = 105$, corresponding to an experiment using silicone oil which was carried out in parallel. In both the numerics and the experiment a volume reduction from the cylindrical shape led to a decrease of the critical Reynolds number. It was not clear from the experiment, however, whether the assumption of a two-dimensional oscillatory flow was justified. Chen & Hu (1998) determined the onset of instability for $Pr = 1$, 10 and 50, neglecting gravity. They qualitatively confirmed the strong stabilization of the two-dimensional flow found in experiments for nearly cylindrical volumes. For $Pr = 1$, aspect ratios in the range $1.4 \leqslant \Gamma \leqslant 2.8$, and for volumes which differ less than 20% from cylindrical, the critical mode was found to be singly periodic ($m = 1$) in the azimuthal direction. Likewise, for $Pr = 10$ and 50, $m = 1$ was predicted to be the critical mode in the extended range of aspect ratios ($1 \leqslant \Gamma \leqslant 2.8$) and for a larger range of the volume fraction. Using the same numerical method, these calculations have been extended to low Prandtl numbers by Chen, Hu & Prasad (1999). By an energy-stability analysis Summer *et al.* (2001) computed energy limits $Re_E$ for guaranteed stability of the basic flow under gravity conditions. They compared the numerical results with experimental data from a silicone–oil liquid bridge with $Pr = 70$. Moreover, energy limits for cylindrical zones given earlier (Neitzel *et al.* 1991) were corrected. Yet, most of the newly obtained energy limits $Re_E$ for $Pr = 1$ are significantly higher than corresponding experimental data. Recently, Lappa, Savino & Monti (2001) reported a numerical simulation of the three-dimensional flow in half-zones with $Pr = 0.01$. They considered the dependence of the critical azimuthal wavenumber on the volume and on the aspect ratio.

Despite the above-mentioned efforts the available numerical results for thermocapillary-flow instabilities in non-cylindrical liquid bridges are scarce and do allow a general understanding of the transition to three-dimensional flow. Hydrostatic effects, for example, are insufficiently covered, and no work exists that can explain, in physical terms, the particular changes of the linear stability upon a variation of the liquid volume. Moreover, some of the cited work must be considered with care, because critical Reynolds numbers from different publications do not agree. Possible reasons could be the uncritical use of coarse numerical grids or inappropriate numerical methods, particularly when the Prandtl number is high and thermal boundary layers must be resolved.

The purpose of the present work is two-fold. A major aim is to cover the parameter space more systematically in order to identify the factors which significantly influence the stability of the two-dimensional flow. To that end the critical Reynolds numbers and the most dangerous perturbation modes will be calculated by a linear stability analysis, and the effect of the Prandtl number, aspect ratio, volume fraction and gravity on the critical Reynolds number will be studied. Another objective is the physical understanding of the instabilities that arise. This problem is treated by carefully considering the local and global energy budgets of the critical modes.

After the problem formulation in § 2 the numerical methods for the linear-stability analysis are introduced in § 3. Some basic-flow properties are discussed in § 4. Linear-stability results are presented in § 5, which is divided into two parts. The first part (§ 5.1) covers the flow in metallic melts which have a small Prandtl number, $Pr \ll 1$. Transparent model fluids with $Pr > 1$ are treated in § 5.2. Both these subsections have the same structure. After a discussion of the general instability mechanism, the influence of the free-surface shape is discussed for constant aspect ratio and zero gravity. This is followed by an investigation of the effects of gravity which affects the flow by buoyancy and through the hydrostatic interface shape. Finally, the aspect-ratio dependence of $Re_c$ is analysed. Section 6 closes with a summary of the results and a comparison with previous work.

## 2. Problem formulation

We consider the flow of an incompressible Newtonian fluid of density $\rho$ confined to a liquid bridge between two parallel coaxial rigid disks of equal radii $r_i = R$ (cf. figure 1). The length $d$ and the radius $R$ define the aspect ratio $\Gamma = d/R$. Like the classical cylindrical half-zone problem (Kuhlmann 1999) the disks are heated differentially by keeping them at constant temperatures $T_0 \pm \Delta T/2$, where $T_0$ is the mean temperature and $\Delta T$ the temperature difference between the two disks. The liquid volume is bounded radially by a free surface at $r = h(z)$, where $h$ is a unique function of the vertical coordinate $z$.

The heated disks enforce free-surface temperature gradients leading to surface-tension variations which are approximated to linear order by

$$\sigma(T) = \sigma_0 - \gamma(T - T_0), \tag{2.1}$$

with $\sigma_0 = \sigma(T_0)$ and $\gamma = -\partial\sigma/\partial T|_{T=T_0}$. Owing to the thermocapillary effect a fluid motion is induced in the liquid. The flow is governed by the non-dimensional Navier–Stokes, the continuity, and the energy equations in the Boussinesq approximation (in which we implicitly assume a static free-surface shape):

$$Re(\partial_t + \boldsymbol{U}\cdot\nabla)\boldsymbol{U} = -\nabla P + \nabla^2\boldsymbol{U} + \frac{Gr}{Re}Te_z, \tag{2.2a}$$

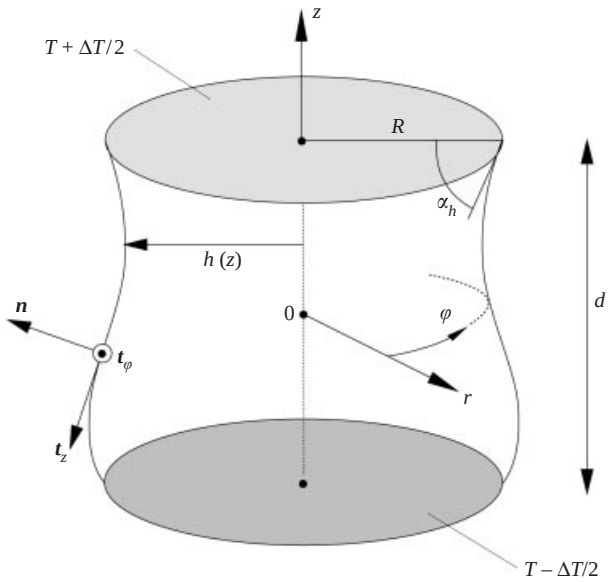


FIGURE 1. Geometry of the liquid bridge.

| Variable | $t$ | $z$ | $r, h$ | $U, V, W$ | $P$ | $T$ | $\mathscr{V}$ | $S$ |
|---|---|---|---|---|---|---|---|---|
| Scale | $d/U^\star$ | $d$ | $R$ | $U^\star = \gamma\Delta T/\rho\nu$ | $\gamma\Delta T/d$ | $\Delta T$ | $\mathscr{V}_{\mathrm{cyl}} = \pi R^2 d$ | $S_{\mathrm{cyl}} = 2\pi R d$ |

TABLE 1. Scaling of the variables. $U^\star$ is the characteristic thermocapillary velocity.

$$\nabla \cdot \boldsymbol{U} = 0, \tag{2.2b}$$

$$Ma(\partial_t + \boldsymbol{U} \cdot \nabla)T = \nabla^2 T, \tag{2.2c}$$

where we use cylindrical coordinates $(r, \varphi, z)$ and the scales for time, lengths, velocity $\boldsymbol{U} = (U, V, W)$, pressure $P$, temperature $T$, and volume of fluid $\mathscr{V}$ given in table 1. $\nabla^2$ is the Laplacian operator. The dimensionless parameters arising in equation 2.2 are the Reynolds, Prandtl, and Grashof numbers

$$Re = \frac{U^\star d}{\nu}, \quad Pr = \frac{\nu}{\kappa}, \quad Gr = \frac{g\beta\Delta T d^3}{\nu^2}, \tag{2.3}$$

where $U^\star$ is the characteristic thermocapillary velocity obtained from balancing thermocapillary and viscous forces, $g$ the acceleration due to gravity, $\nu$ the kinematic viscosity, $\kappa$ the thermal diffusivity, and $\beta$ the thermal expansion coefficient. The Marangoni number is $Ma = Re\ Pr$.

The boundary conditions at the rigid walls of constant temperature are

$$\left.\begin{aligned} \boldsymbol{U} &= 0 \\ T &= \pm 1/2 \end{aligned}\right\} \quad \text{on} \quad z = \pm\tfrac{1}{2}. \tag{2.4a}$$

Uniqueness of the flow fields on the axis requires

$$\left.\begin{aligned} \partial_\varphi U &= V \\ \partial_\varphi V &= -U \\ \partial_\varphi W &= \partial_\varphi T = \partial_\varphi P = 0 \end{aligned}\right\} \quad \text{on} \quad r = 0. \tag{2.4b}$$

The kinematic boundary, tangential-stress and heat-transfer conditions at the free surface are

$$\left.\begin{array}{l} \boldsymbol{n}\cdot\boldsymbol{U}=0 \\ \boldsymbol{t}_z\cdot(\boldsymbol{S}\cdot\boldsymbol{n})=-\boldsymbol{t}_z\cdot\nabla T \\ \boldsymbol{t}_\varphi\cdot(\boldsymbol{S}\cdot\boldsymbol{n})=-\boldsymbol{t}_\varphi\cdot\nabla T \\ \boldsymbol{n}\cdot\nabla T=0 \end{array}\right\} \quad \text{on} \quad r=h(z). \tag{2.4c}$$

The thermocapillary forces must be balanced by viscous tangential stresses, in non-dimensional form $\boldsymbol{S}=\nabla\boldsymbol{U}+(\nabla\boldsymbol{U})^T$, which drive the fluid motion. The ambient gas has been assumed to be inviscid, having negligible density, and the heat transfer into the gas is neglected for simplicity. Some data for the effect of heat transfer can be found in Nienhüser *et al.* (2000).

The vector $\boldsymbol{n}$ is the outward-directed normal vector of the free surface; $\boldsymbol{t}_z$ and $\boldsymbol{t}_\varphi$ denote the unit vectors tangent to the free surface in the $(r,z)$- and $(r,\varphi)$-plane, respectively,

$$\boldsymbol{n}=\mathscr{N}^{-1}(1,0,-h'/\Gamma)^T, \quad \boldsymbol{t}_z=\mathscr{N}^{-1}(h'/\Gamma,0,1)^T, \quad \boldsymbol{t}_\varphi=\boldsymbol{e}_\varphi, \tag{2.5}$$

with the normalizing denominator $\mathscr{N}=(1+h'^2/\Gamma^2)^{1/2}$. Note that the length scales in the radial and axial directions differ, hence $\nabla=[\Gamma\partial_r,(\Gamma/r)\partial_\varphi,\partial_z]$.

Finally, the position $r=h(z)$ of the axisymmetric free surface is determined by static and dynamic forces acting normally to the free surface. Here we consider the asymptotic limit of dominating mean surface tension $\gamma\Delta T\ll\sigma_0$ in which the normal-stress balance can be approximated by the Young–Laplace equation

$$P_s=\nabla\cdot\boldsymbol{n}+Bo\,z, \tag{2.6}$$

with the static Bond number $Bo=\rho g d^2/\sigma_0$. The dimensionless static pressure difference $P_s$ is given in units of $\sigma_0/d$. In the limit (2.6) dynamic deformations of the free surface are suppressed. Hence, the problem (2.6) of determining the shape $r=h(z)$ decouples from the fluid flow. Note that if dynamic surface deformations are to be included, higher corrections to the Boussinesq approximation must be taken into account (Nepomnyashchy & Simanovskii 1995). To solve the second-order equation (2.6) for $h(z)$ we assume fixed contact lines

$$h(z=\pm\tfrac{1}{2})=1. \tag{2.7a}$$

The pressure jump $P_s$ is determined by the additional constraint of either a prescribed fluid volume $\mathscr{V}$ (cf. table 1)

$$\mathscr{V}=\int_{-1/2}^{1/2}h^2(z)\,\mathrm{d}z, \tag{2.7b}$$

or, equivalently, by a fixed hot-wall contact angle $\alpha_h$

$$h'(z=\tfrac{1}{2})=-\tan(\alpha_h-\tfrac{1}{2}\pi). \tag{2.7c}$$

## 3. Numerical methods

### 3.1. *Interface shape*

For capillary number $Ca\to 0$ the free surface is independent of the flow. To obtain the static meniscus shape $h(z)$, (2.6) is written as a system of first-order ordinary

differential equations for the unknowns $h(z)$, $b(z) = h'(z)$, and $P_s$:

$$\left.\begin{aligned} b' &= (\Gamma^2 + b^2)\left[\frac{1}{h} - \frac{(P_s - Boz)}{\Gamma^2}(\Gamma^2 + b^2)^{1/2}\right], \\ h' &= b, \\ P_s' &= 0. \end{aligned}\right\} \tag{3.1}$$

The prime denotes differentiation with respect to $z$. The two-point boundary-value problem (3.1) and (2.7) is solved for a prescribed hot-wall contact angle $\alpha_h$ by a combined shooting and relaxation method using the IMSL subroutines DB2PMS and DB2PFD (VNI 1994). If, instead of $\alpha_h$, the solution for a prescribed volume $\mathscr{V}$ is required, $\alpha_h$ is varied such that (2.7*b*) is satisfied.

### 3.2. *Basic flow*

For small Reynolds numbers the flow in the half-zone is steady and axisymmetric ($\partial_t = \partial_\varphi = V_0 = 0$). This flow is indicated by a subscript 0. Introducing the stream function $\Psi_0$ and the vorticity $\Omega_0$,

$$U_0 = \partial_z \Psi_0, \tag{3.2a}$$

$$W_0 = -\Gamma \mathrm{D}\Psi_0, \tag{3.2b}$$

$$\Omega_0 = \partial_z U_0 - \Gamma\, \partial_r W_0, \tag{3.2c}$$

where $\mathrm{D} \equiv \partial_r + 1/r$, the two-dimensional basic flow $\boldsymbol{U}_0 = (U_0, 0, W_0)$ and $T_0$ must satisfy the equations (curl of (2.2))

$$(\Gamma^2 \partial_r \mathrm{D} + \partial_{zz})\Omega_0 = \Gamma Re\left(\partial_z \Psi_0 \partial_r - \mathrm{D}\Psi_0 \partial_z - \frac{1}{r}\partial_z \Psi_0\right)\Omega_0 + \Gamma \frac{Gr}{Re}\partial_r T_0, \tag{3.3a}$$

$$(\Gamma^2 \mathrm{D}\partial_r + \partial_{zz})T_0 = \Gamma Ma\,(\partial_z \Psi_0 \partial_r - \mathrm{D}\Psi_0 \partial_z)\,T_0, \tag{3.3b}$$

$$(\Gamma^2 \partial_r \mathrm{D} + \partial_{zz})\Psi_0 = \Omega_0. \tag{3.3c}$$

The respective boundary conditions are

$$\Psi_0 = \partial_z \Psi_0 = 0, \quad T_0 = \pm\tfrac{1}{2} \quad \text{on} \quad z = \pm\tfrac{1}{2}, \tag{3.4a}$$

$$\Psi_0 = \Omega_0 = \partial_r T_0 = 0 \quad \text{on} \quad r = 0, \tag{3.4b}$$

and

$$\left.\begin{aligned} &\Psi_0 = 0 \\ &\Omega_0 = -2\frac{h''}{\mathscr{N}^2}\partial_r \Psi_0 + \frac{1}{\mathscr{N}}(h'\partial_r T_0 + \partial_z T_0) \\ &\Gamma\, \partial_r T_0 - \frac{h'}{\Gamma}\partial_z T_0 = 0 \end{aligned}\right\} \quad \text{on} \quad r = h(z). \tag{3.4c}$$

For the numerical solution of (3.3)–(3.4) the cross-section $\varphi = \text{const.}$ for arbitrary axisymmetric free-surface shapes $h(z)$ is mapped to a rectangular domain by

$$\xi = \frac{r}{h}, \quad z = \eta, \qquad \Rightarrow \qquad \partial_r = \frac{1}{h}\partial_\xi, \quad \partial_z = -\xi\frac{h'}{h}\partial_\xi + \partial_\eta. \tag{3.5}$$

In the body-fitted coordinates $(\xi, \eta)$ the free surface is located at $\xi = 1$ (figure 2*a*,*b*). The basic-state equations in body-fitted coordinates are provided in Appendix A.

The transformed system of equations (A 1) and the boundary conditions (A 2) are discretized by second-order finite differences on a non-equidistant grid specified in Appendix A. The resulting nonlinear difference equations are solved by Newton–Raphson iteration with damping. By a proper ordering of the equations the band

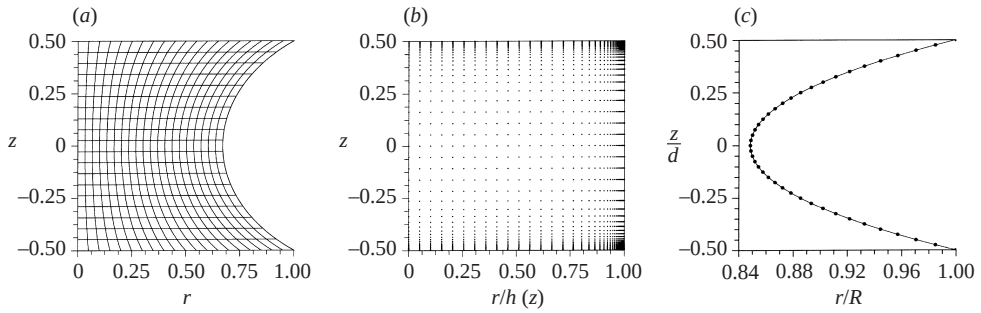


FIGURE 2. (*a*) Isolines of $\xi$ and $\eta$ in the $(r, z)$-plane of a non-cylindrical half-zone. (*b*) Typical distribution of grid points in the $(\xi, \eta)$-plane. (*c*) Free surface shape for $P_s = 0$ and $\Gamma = 1$. —, semi-analytical catenoidal shape; ●: numerical calculation with $N_\eta = 41$ (equidistant mesh).

structure of the Jacobian has been exploited for matrix inversions. Using an implicit LU decomposition and the band-storage mode from the numerical library LAPACK yields significant memory and computing savings.

### 3.3. *Linear stability analysis*

The linear stability of the axisymmetric steady basic state $(U_0, 0, W_0, T_0, P_0)$ with respect to arbitrary three-dimensional perturbations $(u, v, w, \theta, p)$ is governed by the linearized problem (2.2) and (2.4),

$$Re(\partial_t \boldsymbol{u} + \boldsymbol{U}_0 \cdot \nabla \boldsymbol{u} + \boldsymbol{u} \cdot \nabla \boldsymbol{U}_0) = -\nabla p + \nabla^2 \boldsymbol{u} + \frac{Gr}{Re}\theta \boldsymbol{e}_z, \tag{3.6a}$$

$$\nabla \cdot \boldsymbol{u} = 0, \tag{3.6b}$$

$$Ma\,(\partial_t \theta + \boldsymbol{U}_0 \cdot \nabla \theta + \boldsymbol{u} \cdot \nabla T_0) = \nabla^2 \theta. \tag{3.6c}$$

The solutions can be written as normal modes

$$\begin{pmatrix} \boldsymbol{u}(r, \varphi, z, t) \\ \theta(r, \varphi, z, t) \\ p(r, \varphi, z, t) \end{pmatrix} = \begin{pmatrix} \hat{\boldsymbol{u}}(r, z) \\ \hat{\theta}(r, z) \\ \hat{p}(r, z) \end{pmatrix} \mathrm{e}^{\mu t + \mathrm{i}m\varphi} + \text{c.c.}, \tag{3.7}$$

where $m$ is an integer azimuthal wavenumber, $\mu$ the complex growth rate, and c.c. denotes the complex conjugate. We are left to solve (3.6) for the two-dimensional fields $\hat{\boldsymbol{x}} = (\hat{\boldsymbol{u}}, \hat{\theta}, \hat{p})$ for which we apply the same discretization and coordinate mapping as for the basic state.

The details of the resulting equations are given in Appendix B. Here it suffices to note that the discretized system represents a generalized eigenvalue problem of the form

$$\boldsymbol{A}(Re, Ma, Gr, Bi, Bo, \Gamma, \alpha_h; m) \cdot \hat{\boldsymbol{x}}(r_i, z_j) = \mu \boldsymbol{B}(Re, Ma, Bo, \Gamma, \alpha_h) \cdot \hat{\boldsymbol{x}}(r_i, z_j), \tag{3.8}$$

with eigenvalues $\mu$ and eigenvectors $\hat{\boldsymbol{x}}$ composed of the field amplitudes at the grid points. The matrix $\boldsymbol{B}$ is diagonal and singular, while $\boldsymbol{A}$ is a band-structured non-singular matrix. The most dangerous mode, given by the solution of (3.8) with the largest real part of the growth rate, $\max\{\mathrm{Re}(\mu)\}$, is calculated by inverse iteration. The critical Reynolds number $Re_c$ is obtained from the condition $\max\{\mathrm{Re}(\mu)\} = 0$. By inverse iteration the eigenvalue nearest to an initial estimate is accurately detected. The physically relevant modes are identified by using, as a first step, a set of random

initial guesses covering densely the range of reasonable complex growth rates, or by using known growth rates as initial estimates for slightly varied parameters.

### 3.4. *Energetics*

For an understanding of the physics of the instabilities, it is useful to analyse the rates of change of kinetic ($\mathscr{E}_{\mathrm{kin}}$) and 'thermal' energy ($\mathscr{E}_{\mathrm{th}}$)† of the critical perturbation mode. The energy-change rates are obtained by multiplying (3.6*a*) and (3.6*c*) by $\boldsymbol{u}$ and $\theta$, respectively, and integrating over the volume occupied by the liquid. After some algebra, kinetic and thermal energy balances normalized by the mechanical and thermal dissipation $D_{\mathrm{kin}}$ and $D_{\mathrm{th}}$, respectively, can be written in the form

$$\frac{1}{D_{\mathrm{kin}}}\frac{\mathrm{d}}{\mathrm{d}t}\mathscr{E}_{\mathrm{kin}} = \frac{1}{D_{\mathrm{kin}}}\int \boldsymbol{u}\cdot\frac{\partial}{\partial t}\boldsymbol{u}\,\mathrm{d}\mathscr{V} = -1 + \sum_{i=1}^{5} I_i + M_r + M_\varphi + M_z + B, \tag{3.9a}$$

$$\frac{1}{D_{\mathrm{th}}}\frac{\mathrm{d}}{\mathrm{d}t}\mathscr{E}_{\mathrm{th}} = \frac{1}{D_{\mathrm{th}}}\int \theta\frac{\partial}{\partial t}\theta\,\mathrm{d}\mathscr{V} = -1 + \sum_{i=1}^{2} J_i, \tag{3.9b}$$

where $M_r$, $M_\varphi$, and $M_z$ denote the work done by thermocapillary forces per unit time. The work per time done by buoyant forces is $B$. The terms $\sum I_i = -Re/D_{\mathrm{kin}}\int \boldsymbol{u}\cdot(\boldsymbol{u}\cdot\nabla)\boldsymbol{U}_0\mathrm{d}\mathscr{V}$ and $\sum J_i = -Ma/D_{\mathrm{th}}\int \theta(\boldsymbol{u}\cdot\nabla)T_0\mathrm{d}\mathscr{V}$ describe the relative mechanical and thermal production rates due to convective transport of basic-state momentum and temperature, respectively, by the perturbation velocity field. The individual terms in the sums arise from the particular decomposition, e.g. into cylindrical coordinates, of the flow fields. Detailed expressions for all contributions can be found in Appendix C. For a discussion of the instability mechanisms it is helpful to investigate the local distributions (densities $i_i$ and $j_i$) of the integral terms $I_i$ and $J_i$, which are defined by $I_i = \int i_i\mathrm{d}\mathscr{V}$ and $J_i = \int j_i\mathrm{d}\mathscr{V}$.

To evaluate the energy balances, the derivatives appearing in (3.9) are formulated in analogy to the discretization of the basic-state and the linear-stability equations, and all integrals are approximated using Simpson's rule.

### 3.5. *Code validation*

To validate the calculation of the liquid-bridge shape we consider the catenoidal profile $h^{\mathrm{cat}}(z)$:

$$h^{\mathrm{cat}}(z) = h_0\cosh\left(\frac{\Gamma}{h_0}z\right), \quad \text{with} \quad h_0\cosh\left(\frac{\Gamma/2}{h_0}\right) = 1, \tag{3.10}$$

which is an exact solution of the static meniscus problem (2.6) and (2.7) for zero-gravity conditions (see e.g. Padday 1976). From (3.10) and for $\Gamma = 1$ one obtains the minimum radius $h_0 = h|_{z=0} \approx 0.8483379380$. Since the mean curvature and hence the static pressure difference is exactly zero for catenoidal shapes, we solve (2.6) with the boundary conditions (2.7*a*) and $P_{\mathrm{s}} = 0$. The result very accurately matches the catenoid (cf. figure 2*c*). In particular, the numerically computed minimum radius is $h_0 = 0.848337939$ with a relative error of $10^{-9}\%$.

In a next step, the basic-flow and linear-stability codes have been validated by grid-refinement studies, comparison with existing data, and by checking the energy conservation. To verify the basic state, some minimum values of the Stokes stream

† The 'thermal' energy must not be confused with the thermodynamic thermal energy. $\mathscr{E}_{\mathrm{th}}$ is merely a measure for the temperature deviation from the basic temperature field, defined in analogy to $\mathscr{E}_{\mathrm{kin}}$.

| | | $Pr = 0.02$ | | $Pr = 4$ | |
|---|---|---|---|---|---|
| | $N_\xi \times N_\eta$ | $\min \Psi^{\mathrm{St}} \times 10^3$ | $\delta Nu$ | $\min \Psi^{\mathrm{St}} \times 10^3$ | $\delta Nu$ |
| Leypoldt *et al.* (2000) | | −6.31 | | −1.95 | |
| Present (E) | 41 × 41 | −5.76 | 0.016 | −1.69 | 0.22 |
| Present (E) | 81 × 81 | −6.21 | 0.005 | −1.94 | 0.04 |
| Present (E) | 161 × 161 | −6.32 | 0.002 | −2.03 | 0.008 |
| Present (NE/40) | 89 × 137 | −6.23 | 0.003 | −2.03 | 0.008 |
| Present (NE/80) | 122 × 163 | −6.28 | 0.001 | −2.03 | 0.003 |

TABLE 2. Minimum values of the Stokes stream function and relative error in the total Nusselt number of the basic flow for different Prandtl numbers for a cylindrical liquid bridge and $Re = 5000$, $\Gamma = 1$, $Gr = 0$. Equidistant grids (E) and non-equidistant grids with $f = 1.1$, $\Delta^{\min} = 10^{-4}$ and $\Delta^{\max} = 1/40$ (NE/40) and $\Delta^{\max} = 1/80$ (NE/80).

function $\Psi_0^{\mathrm{St}} = r\Psi_0$ for different grids $N_\xi \times N_\eta$ are compared with literature data in table 2. Convergence is obtained for sufficiently fine grids, the converged values being in good agreement with the reference data. In addition, the Nusselt numbers for the heat transfer through the hot and cold walls, $Nu_{\mathrm{h}}$ and $Nu_{\mathrm{c}}$ (the free-surface Nusselt number $Nu_{\mathrm{sf}}$ is zero here), have been computed. They and the corresponding heat currents $F_i$ are defined as (dimensional quantities)

$$Nu_i = \frac{F_i}{k(\Delta T/d)\pi R^2}, \qquad F_i = -k \int_{S_i} \frac{\partial T}{\partial z} \mathrm{d}S, \qquad i \in [\mathrm{h}, \mathrm{c}], \tag{3.11}$$

where $k$ is the thermal conductivity of the liquid. Since $Nu_{\mathrm{h}} + Nu_{\mathrm{c}}$ vanishes with a relative error $\delta Nu = \sum_i Nu_i / \max |Nu_i|$ which is less than 1% throughout, we find that the thermal energy of the basic state is very accurately conserved for all calculations presented.

Finally, for a validation of the linear stability analysis, we have successfully compared our critical data with those for cylindrical liquid bridges published by Wanschura (1996). Quantitative comparisons are provided in § 5.1 and 5.2. In addition, the consistency of the linear stability analysis has been proven by checking the energy conservation (C 6) of the neutral modes. We found that the error $\delta E_{\mathrm{kin}}$ is less than 5% and $\delta E_{\mathrm{th}}$ is less than 1% for small Prandtl numbers ($Pr < 1$). For high Prandtl numbers ($Pr > 1$) and large interface deflection a precise resolution of the perturbation flow in the singular corners requires an extremely fine mesh (Kuhlmann, Nienhüser & Rath 1999). To circumvent this problem, we consider a regularized version of the linear stability problem for $Pr > 1$ in which the thermocapillary boundary conditions at the free surface are smoothly matched with the rigid boundary condition at the heated walls (cf. Kasperski & Labrosse 2000). This is accomplished by replacing the second and third equations of (2.4*c*) by Robin-type mixed conditions

$$\boldsymbol{t}_z \cdot (\boldsymbol{S} \cdot \boldsymbol{n}) = -f(\eta)\boldsymbol{t}_z \cdot \nabla\theta - g(\eta)\boldsymbol{t}_z \cdot \boldsymbol{u}, \tag{3.12}$$

$$\boldsymbol{t}_\varphi \cdot (\boldsymbol{S} \cdot \boldsymbol{n}) = -f(\eta)\boldsymbol{t}_\varphi \cdot \nabla\theta - g(\eta)\boldsymbol{t}_\varphi \cdot \boldsymbol{u}, \tag{3.13}$$

where

$$f(\eta) = \begin{cases} \frac{1}{4}[1 - \cos((\eta - \frac{1}{2})\pi/s)]^2, & \eta \leqslant -\frac{1}{2} + s \\ 1, & -\frac{1}{2} + s < \eta < \frac{1}{2} - s \\ \frac{1}{4}[1 - \cos((\frac{1}{2} - \eta)\pi/s)]^2, & \eta \geqslant \frac{1}{2} - s, \end{cases} \tag{3.14}$$

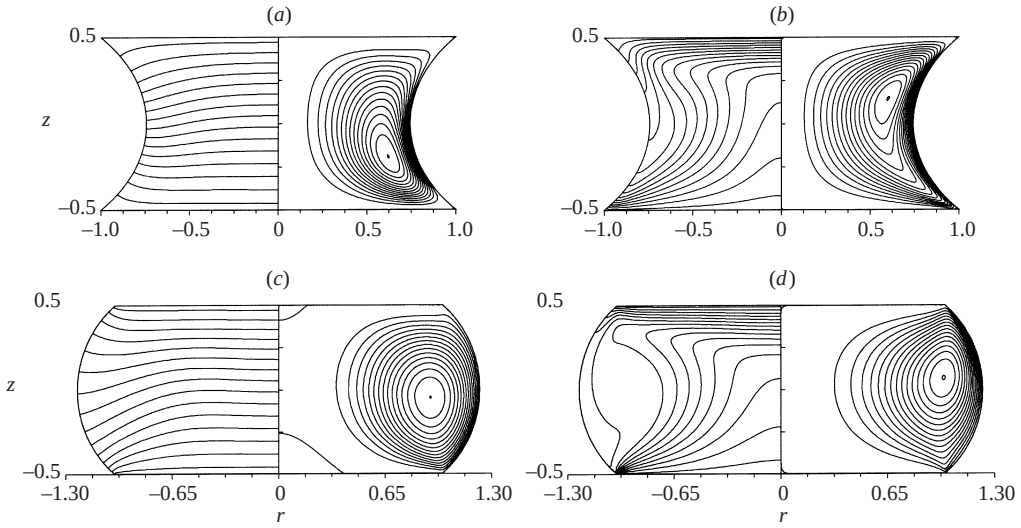


FIGURE 3. Isotherms (left) and streamlines (right) of the two-dimensional flow for $Bo = Gr = 0$ and $\Gamma = 1$. (*a*) $Pr = 0.02$, $Re = 2000$, $\alpha = 40°$; (*b*) $Pr = 4$, $Re = 800$, $\alpha = 40°$; (*c*) $Pr = 0.02$, $Re = 2000$, $\alpha = 140°$; (*d*) $Pr = 4$, $Re = 800$, $\alpha = 140°$.

and

$$g(\eta) = \begin{cases} \operatorname{arc\,tanh}^4 (1 - f(\eta)), & \eta \leqslant -\frac{1}{2} + s \\ 0, & -\frac{1}{2} + s < \eta < \frac{1}{2} - s \\ \operatorname{arc\,tanh}^4 (1 - f(\eta)), & \eta \geqslant \frac{1}{2} - s. \end{cases} \tag{3.15}$$

Note that the basic flow is not regularized and experiences the full Marangoni driving force. A regularization within 0.2% of the free surface ($s = 0.002$) is kept throughout for all linear stability calculations and $Pr > 1$, unless noted otherwise. The linear stability boundaries of the unregularized system ($s = 0$) always differ by less than 5% from those of the regularizated system ($s = 0.002$). Thus the relative error $\delta E_{\mathrm{th}}$ is less than 1%, while $\delta E_{\mathrm{kin}}$ is less than 10%.

Finally, grid-parameter convergence was tested by variation of the grid-stretching factors $f$ and the minimum ($\Delta^{\min}$) and the maximum ($\Delta^{\max}$) grid spacings. Most rapid convergence has been obtained by using grids satisfying $1.09 \leqslant f \leqslant 1.2$, $5 \times 10^{-5} \leqslant \Delta^{\min} \leqslant 5 \times 10^{-4}$, and $0.02 \leqslant \Delta^{\max} \leqslant 0.03$. Corresponding data for different contact angles and Prandtl numbers are given in the respective sections together with published reference data, whenever available. Typically, the number of radial grid points varies in the range $N_\xi \approx 40 \ldots 100$, while the number of axial points is $N_\eta \approx 61 \ldots 141$.

## 4. Basic two-dimensional flow

The steady axisymmetric flows represent a parametric input to the linear stability analysis. We briefly describe the characteristic properties of these flows as functions of the contact angle $\alpha_h$ and the Prandtl number. The dependence on the volume fraction $\mathscr{V}$ is similar and can be inferred from figure 24 and table 10 in Appendix D. For simplicity, gravity is neglected ($Gr = Bo = 0$). For zero-gravity conditions the free-surface shape is symmetric with respect to $z = 0$ and the cold-disk contact

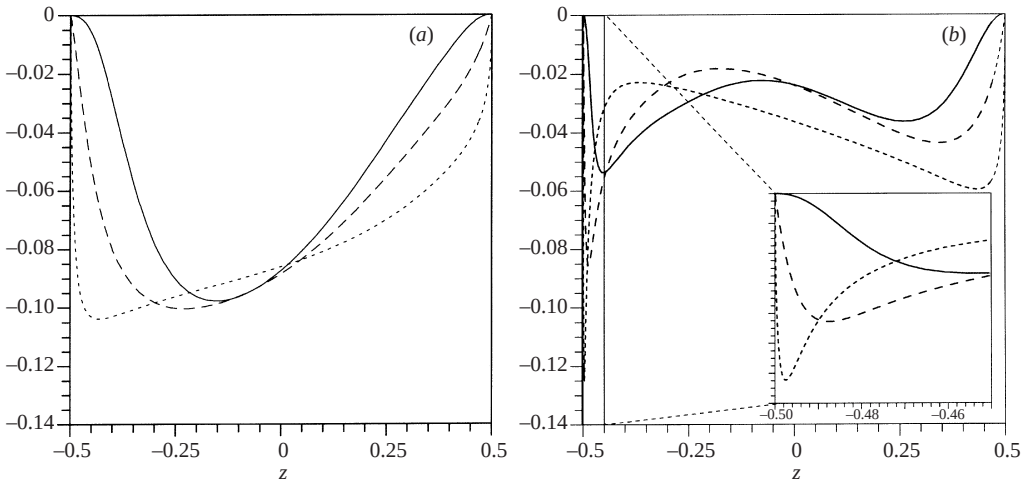


FIGURE 4. Basic-state velocities on the free surface for different contact angles and $Bo = Gr = 0$, $\Gamma = 1$: $\alpha = 40°$ (—), $\alpha = 90°$ (– –), $\alpha = 140°$ (- - -). (*a*) $Pr = 0.02$, $Re = 2000$, (*b*) $Pr = 4$, $Re = 800$.

angle equals that of the hot-disk, $\alpha = \alpha_c = \alpha_h$. Figure 3 shows the isotherms and streamlines for a representative small ($\alpha = 40°$) and large contact angle ($\alpha = 140°$) as well as for a small ($Pr = 0.02$) and a large Prandtl number ($Pr = 4$) for unit aspect ratio $\Gamma = 1$. Owing to the insulating free surface the isotherms are perpendicular to the free surface. Hence, the free-surface temperature gradients near the corners are reduced for slender liquid bridges, $\alpha < 90°$, while they are enhanced for $\alpha > 90°$. Typical velocity profiles on the free surface are shown in figure 4. The convective transport leads to strong temperature gradients near the cold corner. This crowding of isotherms is significantly promoted by large contact angles. In particular, the asymptotic scaling of the velocity field as a function of the distance from the corners changes and the velocity gradients at the corners increase progressively with $\alpha$ when $\alpha > 128.7°$ (Kuhlmann *et al.* 1999). Nevertheless, the conductive–viscous ($W_0^{\min} \sim Re^0$) and the conductive–inertial scaling ($W_0^{\min} \sim Re^{-1/3}$) of the velocity peak $W_0^{\min}$ near the cold wall predicted by Canright (1994) for low Prandtl numbers is approximately confirmed for $Pr = 0.02$ (not shown).

For convex shapes ($\alpha > 90°$), the single vortex centre is shifted radially outward and towards the mid-plane $z = 0$. As shown in figure 3 the vortex centre is shifted radially inward and towards the hot wall (high $Pr$) or the cold wall (low $Pr$) on a decrease of $\alpha$, as in cylindrical bridges (see e.g. Kuhlmann 1999, pp. 84–86). In addition, the basic vortex becomes more stretched when decreasing the contact angle for both $Pr = 0.02$ and $Pr = 4$. For high volume fraction $\mathscr{V}$ the streamlines become more circular. This feature, together with the enlarged free surface area, leads to a strengthening of the vortex indicated by an increase in the absolute value of the stream-function extremum at the vortex core visible in figure 5.

When the aspect ratio is increased for constant contact angle the toroidal vortex becomes elongated and a hyperbolic stagnation point may appear (figure 6). This stagnation point separates two distinct regions of recirculation embedded in a globally circulating flow. This property has been observed before in cavity Stokes flow by Kelmanson & Lonsdale (1996), but can also result from a spatial instability (Laure, Roux & Ben Hadid 1990). Here, the appearance of a hyperbolic stagnation point is assisted by small contact angles which promote a narrowing of the bridge. Since this

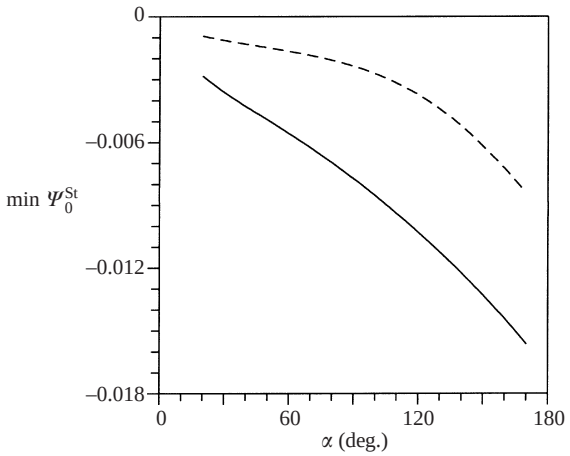


FIGURE 5. Minimum value of the basic-state stream function as a function of the contact angle $\alpha$ for $Bo = Gr = 0$, $\Gamma = 1$: $Pr = 0.02$, $Re = 2000$ (—), $Pr = 4$, $Re = 1000$ (– –).

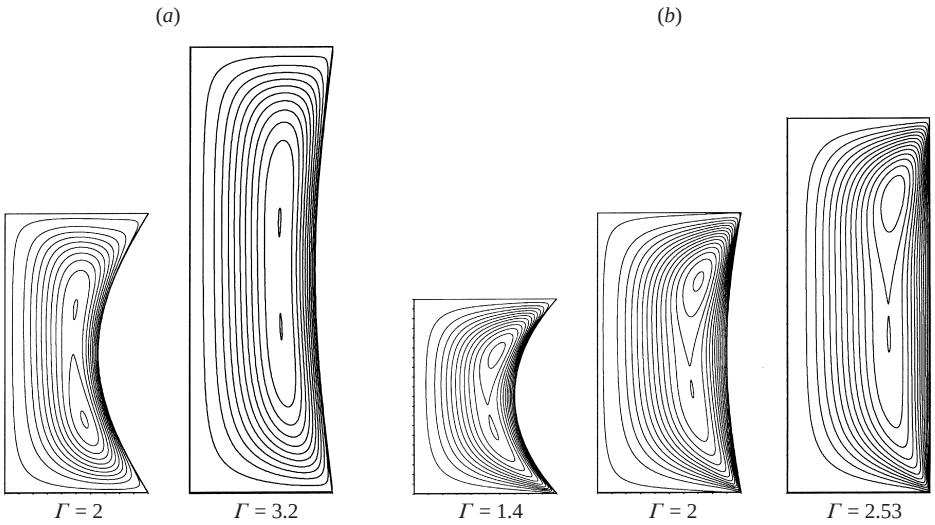


FIGURE 6. Streamlines illustrating the existence of a hyperbolic stagnation point at aspect ratios slightly above the values given in table 3. (*a*) $Pr = 0.02$, $Re = 2000$, $\alpha = 40°$, $70°$. (*b*) $Pr = 4$, $Re = 800$, $\alpha = 40°$, $70°$, $90°$.

behaviour represents a qualitative change in the flow topology, we give, in table 3, some typical aspect ratios above which a hyperbolic stagnation point exists in the flow.

## 5. Stability of two-dimensional flows

It has been shown by Wanschura *et al.* (1995) that two distinct instabilities of the two-dimensional flows exist in cylindrical thermocapillary liquid bridges. For small Prandtl numbers ($Pr \lesssim 0.1$) the instability is stationary, whereas it is oscillatory for high Prandtl numbers ($Pr \gtrsim 1$) (see also Chen, Lizée & Roux 1997). For this reason, we consider these instabilities separately. If not mentioned otherwise, all calculations

| $\alpha$ (deg.) | $Pr = 0.02$ $Re = 2000$ | $Pr = 4$ $Re = 800$ |
|---|---|---|
| 40 | 1.93 | 1.34 |
| 70 | 3.11 | 1.98 |
| 90 | $> 2\pi$ | 2.51 |

TABLE 3. Aspect ratio $\Gamma$ as function of the contact angle at which a hyperbolic stagnation point appears in the basic flow ($Bo = Gr = 0$).

| | $\alpha = 30°$ | $\alpha = 50°$ | | $\alpha = 90°$ | $\alpha = 130°$ |
|---|---|---|---|---|---|
| $N_\xi \times N_\eta$ | $m = 1$ | $m = 1$ | $m = 2$ | $m = 2$ | $m = 2$ |
| $59 \times 81$ | 3949 | 2772 | 2545 | 2293 | 3331 |
| $72 \times 97$ | 3457 | 2672 | 2473 | 2152 | 3249 |
| $92 \times 121$ | 3281 | 2611 | 2434 | 2109 | 3181 |
| $119 \times 157$ | 3222 | 2584 | 2422 | 2087 | 3112 |
| extrapolated | 3070 | 2540 | 2380 | 2060 | 3070 |
| Wanschura *et al.* (1995) | | | | 2062 | |

TABLE 4. Neutral Reynolds numbers $Re_c(m)$ for $Pr = 0.02$ and different contact angles $\alpha$. Results for different grids are shown together with the value obtained by Richardson extrapolation using the r.m.s. value of the grid spacing. The parameters are $\Gamma = 1$, $Bo = Gr = 0$.

are performed for $Gr = Bo = 0$, and $\Gamma = 1$. Due to the mirror symmetry with respect to $z = 0$ of (2.6), and hence of $h(z)$, when $Bo = 0$ we have $\alpha = \alpha_c = \alpha_h$.

### 5.1. *Low Prandtl numbers*

The critical curve for the stationary instability of the axisymmetric toroidal basic flow at low Prandtl numbers evolves continuously with the contact angle. After having verified, using complex arithmetic, that the growth rate is real ($\mathrm{Im}(\mu) = 0$), all successive computations were performed with real arithmetic for computational economy. By solving the purely axisymmetric stability problem it was ensured, moreover, that no instability occurs with $m = 0$ for the parameters used. The typical convergence of the critical Reynolds number is given in table 4. Furthermore, we compare our critical Reynolds numbers with those given by Chen *et al.* (1999) in table 5. Except for $Pr = 0.01$, $\gamma = 0.8$, both results are in a reasonable agreement with a maximum deviation of $\approx 10\%$. Lappa *et al.* (2001) determined the critical Reynolds number for $Pr = 0.01$, $\gamma = 1.0$ by direct numerical simulation: the obvious disagreement with the present result and the value given by Chen *et al.* (1999) may suggest a too coarse numerical grid.

#### 5.1.1. *General remarks on the instability mechanism*

Wanschura *et al.* (1995) have shown that the instability mechanism for low-Prandtl-number cylindrical liquid bridges is essentially inertial. An *a posteriori* evaluation of the kinetic energy balance confirms this mechanism, and also for deformed interfaces. Hence the instability is independent of $\alpha$. As shown in figure 7(*a*) the dissipation $D_{\mathrm{kin}}$ of the perturbation flow is balanced by the total production $\sum I_i$. Work done by Marangoni forces is negligible for the kinetic energy budget. The total local production $\boldsymbol{u} \cdot (\boldsymbol{u} \cdot \nabla)\boldsymbol{U}_0 = \sum I_i$ is shown in figure 7(*b*, *c*) for a cylindrical half-zone. Two main regions of high energy gain are visible. One amplification peak is located

| $Pr$ | $\mathscr{V}$ | $m_c$ | Present $Re_c$ | Chen *et al.* (1999) $Re_c$ | Lappa *et al.* (2001) $Re_c$ |
|---|---|---|---|---|---|
| 0.001 | 0.6 | 1 | 3420 | 3130 | |
| 0.001 | 0.8 | 2 | 2020 | 1990 | |
| 0.001 | 1.0 | 2 | 1650 | 1560 | |
| 0.001 | 1.2 | 2 | 1850 | 1810 | |
| 0.01 | 0.6 | 1 | 2780 | 2810 | |
| 0.01 | 0.8 | 2 | 2200 | 1880 | |
| 0.01 | 1.0 | 2 | 1770 | 1550 | 2500 |
| 0.01 | 1.2 | 2 | 2030 | 1810 | |

TABLE 5. Critical Reynolds numbers $Re_c$ for $Pr = 0.001$ and $Pr = 0.01$ as well as for different volume fractions $\mathscr{V}$ and $\Gamma = 1.2$, $Bo = Gr = 0$.

near the centre of the basic vortex. The second region of energy supply extends from the cold corner to the hot wall stretched along the basic flow streamlines.

A deeper understanding of the underlying mechanism can be obtained by decomposing the local production term $\boldsymbol{u}\cdot(\boldsymbol{u}\cdot\nabla)\boldsymbol{U}_0$ into different components. The result of Wanschura *et al.* (1995) who used cylindrical coordinates (Appendix C), is recovered in figures 8(*a*) (dark grey bars) and 8(*b*). In this decomposition the most destabilizing term appears to be $I_4 = -Re\int_V \hat{w}\hat{u}\partial_r W_0$. The local distribution of $\int i_4\, r\mathrm{d}\varphi$ is shown in figure 8(*b*). Comparing with figure 7(*b*), $i_4$ represents well the peak of $\int \sum i_i\, r\mathrm{d}\varphi$ near the centre of the vortex, but fails to capture the second region of destabilization (figure 7*b*, *c*).

Alternatively, the perturbation velocity can be decomposed into components parallel and perpendicular to the basic flow (Albensoeder, Kuhlmann & Rath 2000):

$$\boldsymbol{u}_\parallel = \frac{(\boldsymbol{u}\cdot\boldsymbol{U}_0)\boldsymbol{U}_0}{\boldsymbol{U}_0^2}, \qquad \boldsymbol{u}_\perp = \boldsymbol{u} - \boldsymbol{u}_\parallel, \tag{5.1}$$

which yields the total normalized production

$$\sum_{i=2}^{5} I_i = \sum_{i=2}^{5} I_i' = \frac{Re}{|D_{\mathrm{kin}}|}\int_{\mathscr{V}} [-\boldsymbol{u}_\perp\cdot(\boldsymbol{u}_\perp\cdot\nabla\boldsymbol{U}_0) - \boldsymbol{u}_\perp\cdot(\boldsymbol{u}_\parallel\cdot\nabla\boldsymbol{U}_0) - \boldsymbol{u}_\parallel\cdot(\boldsymbol{u}_\perp\cdot\nabla\boldsymbol{U}_0) - \boldsymbol{u}_\parallel\cdot(\boldsymbol{u}_\parallel\cdot\nabla\boldsymbol{U}_0)]\,\mathrm{d}\mathscr{V}. \tag{5.2}$$

The total energy budget using this decomposition is shown in figure 8(*a*) (light grey bars). As can be seen from figure 8(*c*), the sum of the two local production terms $\int i_3' + i_4'\, r\mathrm{d}\varphi$ reproduces nearly perfectly the second region of amplification aligned with the basic streamlines in figure 7(*b*). The amplification peak near the centre of the vortex, however, is not caused by these terms.

The dominant term $I_4'$ represents the energy production by amplification of streamwise perturbation flow due to transport of basic-state momentum perpendicular to the base-flow direction (the so-called lift-up mechanism). In the case of circular Couette flow with the inner cylinder rotating, the angular momentum decreases radially outward and the process associated with $I_4'$ is responsible for the centrifugal instability leading to Taylor-vortex flow (cf. Drazin & Reid 1981). In the present case, the streamlines in the region of amplification are convex, but are not circular. Bayly (1986), however, has generalized the Rayleigh criterion (Rayleigh 1916) to inviscid flows with closed convex streamlines. He derived a sufficient condition for centrifugal

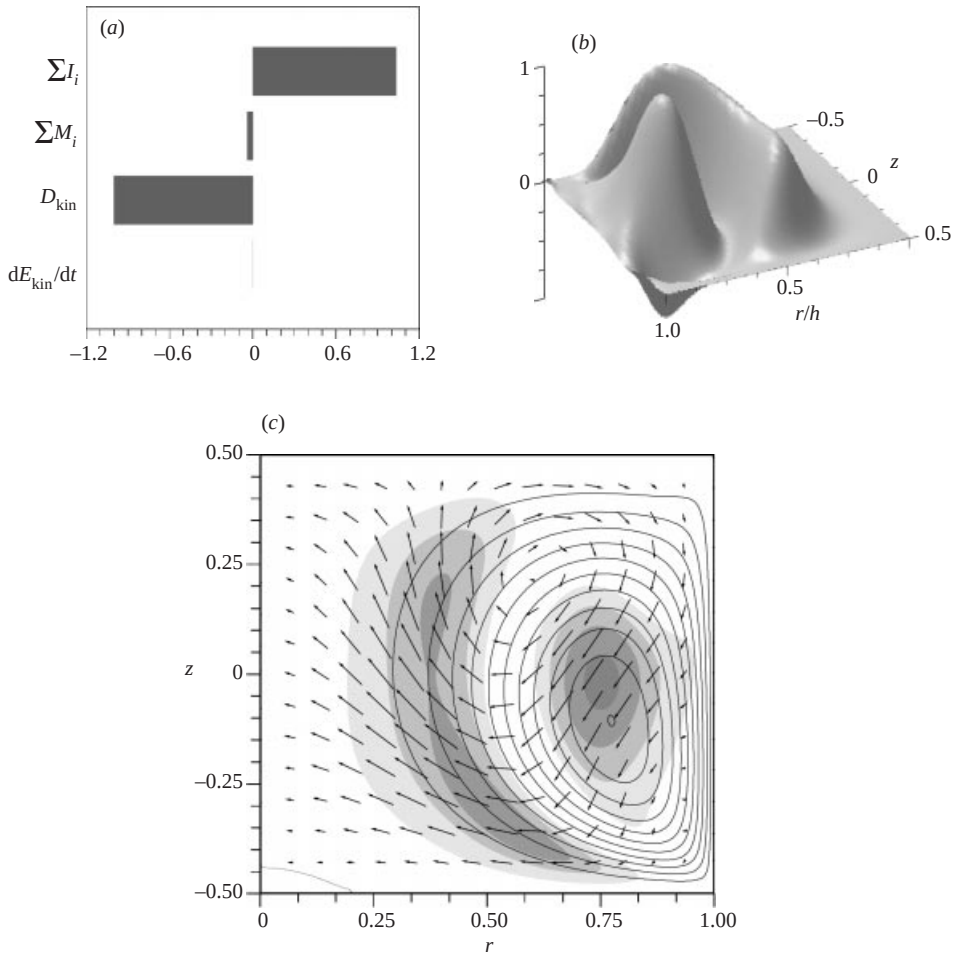


FIGURE 7. (*a*) Kinetic energy balance of the critical mode for $\alpha = 90^\circ$ and $Pr = 0.02$, $\Gamma = 1$, $Re_c = 2130$, $m = 2$, and $Bo = Gr = 0$; (*b*) total local production $\sum \int i_i \, r \mathrm{d}\varphi$; (*c*) regions of high production (shaded) together with the basic stream function (isolines) and the critical velocity field (vectors).

instability when the circulation along a closed streamline decreases radially outward. There is no strict mathematical criterion for the existence of a centrifugal instability in viscous flows. However, the circulation $\tilde{\Gamma} = \oint \boldsymbol{U}_0 \cdot \mathrm{d}\boldsymbol{s}$ decreases radially outward for the outer streamlines. Figure 9 shows the circulation as a function of the normalized *mean radius* from the vortex centre $\bar{r}_{\mathrm{cs}}/\bar{r}_{\mathrm{cb}}$, defined as

$$\bar{r}_{\mathrm{cs}} = \frac{\oint r_{\mathrm{cs}} \, \mathrm{d}s}{\oint \mathrm{d}s}, \qquad \bar{r}_{\mathrm{cb}} = \frac{\oint r_{\mathrm{cb}} \, \mathrm{d}\partial A}{\oint \mathrm{d}\partial A}.$$

Here, $r_{\mathrm{cs}}$ and $r_{\mathrm{cb}}$ denote the distance from the vortex centre, where the Stokes stream function takes its minimum, to the streamline $s$ and to the boundary of the domain $\partial A$, respectively. For all Reynolds numbers we find that the magnitude of the circulation decreases radially for sufficiently large radii. This indicates a centrifugal instability mechanism.

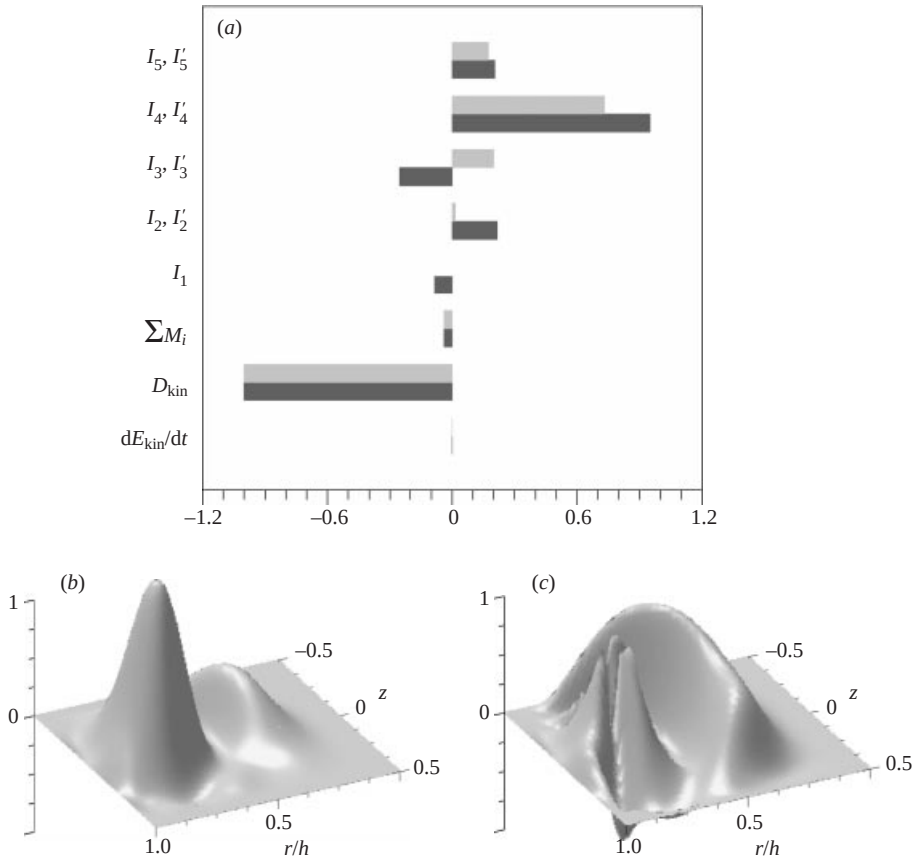


FIGURE 8. (*a*) Kinetic energy balance using decompositions of $\boldsymbol{u}$ into cylindrical ($I_i$, dark grey) and local coordinates ($I_i'$, light grey). (*b*, *c*). The local production terms $\int i_4\, r\mathrm{d}\varphi$ (*b*) and $\int (i_3' + i_4')\, r\mathrm{d}\varphi$ (*c*) for the flow in a cylindrical half-zone with $Pr = 0.02$, $\Gamma = 1$, $Re_c = 2130$, $m = 2$, and $Bo = Gr = 0$.

We conclude that two different mechanisms are responsible for the inertial instability at low Prandtl numbers. The first contribution $I_4$ is due to the strain in the vortex centre near the free surface (Wanschura *et al.* 1995; Levenstam & Amberg 1995). A second contribution, not reported previously, is due to centrifugal effects represented by $I_4'$. In the following sections we investigate how the shape of the liquid bridge affects these two instability mechanisms.

### 5.1.2. *Volume-of-fluid effects*

The influence of the free-surface shape on the critical Reynolds numbers is investigated by varying the contact angle and keeping the Prandtl number constant. Figure 10(*a*) shows the neutral curves for $Pr = 0$, 0.02 and 0.04. The critical wavenumber is either $m_c = 1$ or $m_c = 2$. Additional calculations (not shown) confirm that the neutral Reynolds numbers $\mathrm{Re}_c(m)$ with $m > 2$ are always larger than those given in figure 10(*a*). The critical wavenumber for slender liquid bridges and $\Gamma = 1$ is $m_c = 1$. On an increase in the contact angle $\alpha$ the wavenumber changes to $m_c = 2$. When the Prandtl number is increased from zero, the contact angle of the cross-over point also increases. For larger $Pr$ the ($m = 1$) curve may even reach a local minimum before it intersects with the ($m = 2$)-branch. The global minimum of the envelope of the

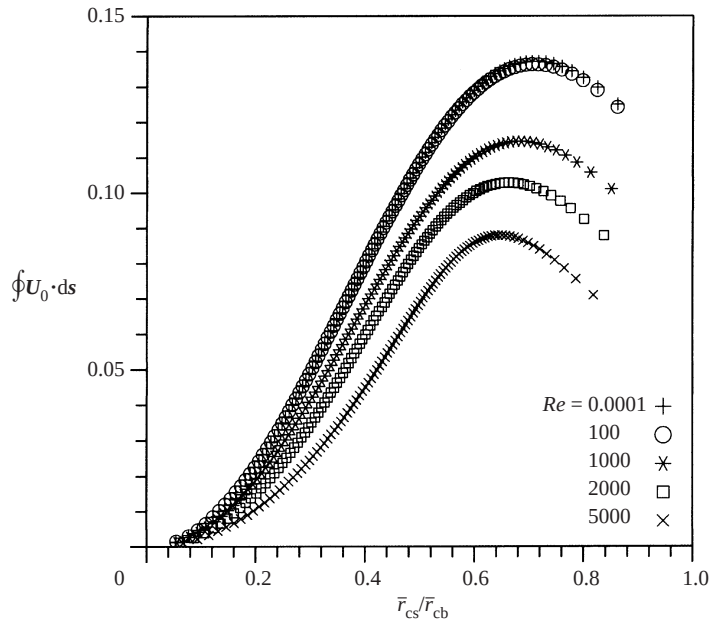


FIGURE 9. Circulation $\tilde{\Gamma}$ along closed streamlines of the two-dimensional basic flow as function of the relative mean radius for cylindrical liquid bridges and for different Reynolds numbers indicated by symbols. $Pr = 0.02$, $\Gamma = 1$, and $Bo = Gr = 0$.

| $Pr$ | $\alpha^{\min}$ (deg.) | $Re_c(\alpha^{\min})$ | $\alpha^{\star}$ (deg.) |
|---|---|---|---|
| 0 | 77 | 1800 | 36 |
| 0.02 | 79 | 2090 | 44 |
| 0.04 | 74 | 2850 | 58 |

TABLE 6. Minimum critical Reynolds numbers $Re_c$ for $Pr = 0$, 0.02, and 0.04 as function of $\alpha$ for $\Gamma = 1$, $Bo = Gr = 0$ together with the corresponding $\alpha^{\min}$ and the contact angle $\alpha^{\star}$ at which the critical wavenumber changes from $m_c = 1$ to $m_c = 2$.

neutral curves occurs for moderately concave surface shapes and for $m = 2$. Some characteristic quantitative data are given in table 6. Note that the general behaviour indicated in figure 10($a$) only holds up to $Pr \approx 0.055$ beyond which the critical curve becomes more complicated (Levenstam, Amberg & Winkler 2001).

It is well known that the critical wavenumber for $Bo = 0$ and $\alpha = 90^{\circ}$ scales with the aspect ratio approximately like $m_c \simeq 2/\Gamma$ (Preisser, Schwabe & Scharmann 1983, experiments for large $Pr$; and Levenstam & Amberg 1995, and Wanschura *et al.* 1995, numerics for small $Pr$). Thus the change from $m_c = 2$ to $m_c = 1$ upon a decrease in $\alpha$ (figure 10$a$) may be interpreted here as an increase in the *effective* aspect ratio.

The kinetic energy balance of the most dangerous mode is shown in figure 10($b$) for a constant Reynolds number $Re = 2130 = Re_c^{\mathrm{cyl}}$. For all contact angles the instability is inertial and Marangoni work is insignificant. To elucidate the influence of the contact angle $\alpha$ on the instability, we consider both the basic vortex and the perturbation flow field at constant $\varphi = \varphi_0$ together with the total local production $\int \sum i_i \, r \mathrm{d}\varphi$ for a constant Reynolds number $Re = 2130$ and for a constant wavenumber $m = m_c(\alpha = 90^{\circ}) = 2$. In the plane $\varphi = \varphi_0$ defined by a vanishing azimuthal perturbation flow $v(\varphi_0) = 0$, the perturbation velocity field is symmetric with respect

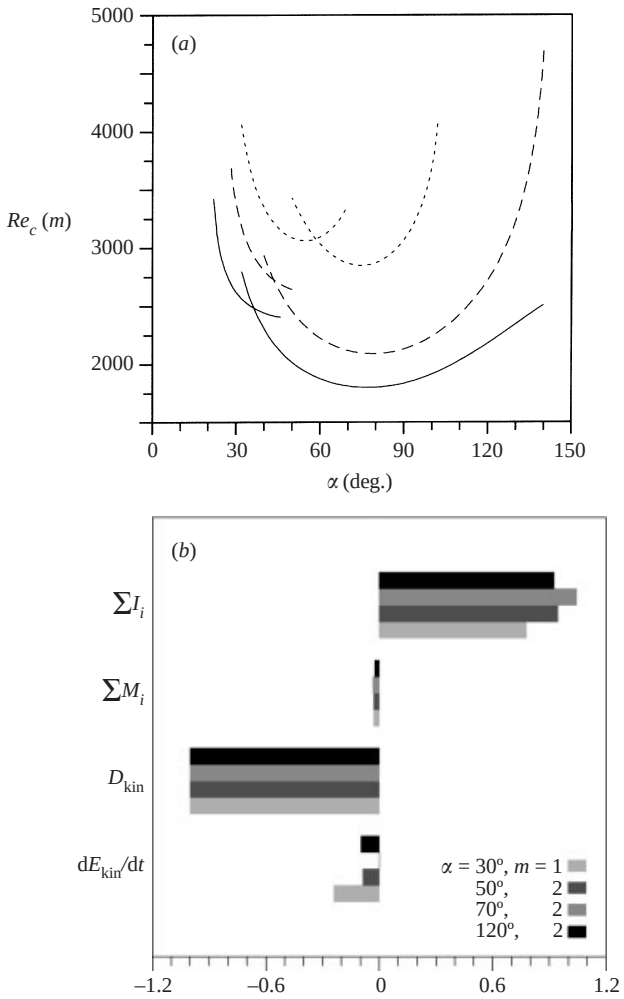


FIGURE 10. (*a*) Curves of neutral stability as function of the contact angle α for different low Prandtl numbers: $Pr = 0$ (—), $Pr = 0.02$ (– –), and $Pr = 0.04$ (- - -). The left curves (low α) correspond to $m_c = 1$ while the right curves (high α) correspond to $m_c = 2$. (*b*) Kinetic energy budget of the most dangerous modes for fixed $Re = 2130 = Re_c^{\rm cyl}$, different contact angles and wavenumbers for $Pr = 0.02$.

to $\varphi - \varphi_0 \rightarrow -(\varphi - \varphi_0)$ and consists of a single vortex. Typical situations are shown in figure 11(*a–c*) for representative contact angles.

At small contact angles ($\alpha = 30^\circ$) the basic vortex is stretched in the axial direction and displaced towards the cold wall. The enhanced strain on the vortex due to the geometrical constraints leads to high values of $\partial_r W_0$ near the vortex centre and hence to a high contribution of the strain-induced instability mechanism. On the other hand, due to the position of the basic vortex and the structure of the neutral mode, the region of centrifugal destabilization is confined to a relatively small region near the cold wall (cf. figure 11*a*). When the contact angle α increases, the basic streamlines become more circular, indicating less strain, and the efficiency of the mechanism in the vortex core is substantially reduced. Now, however, the centrifugal mechanism becomes more important, because the large contact angle and the increased local driving (Kuhlmann *et al.* 1999) promote the vortex flow (figure 11*c*).

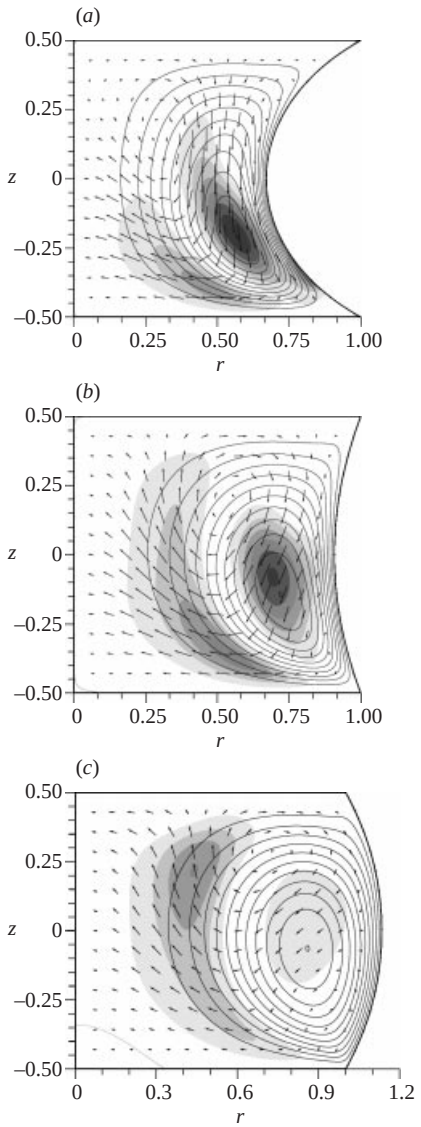


FIGURE 11. Basic-state streamlines, perturbation flow (arrows), and local production $\int \sum i_i r \mathrm{d}\varphi$ (shaded, only the positive contributions are shown) at $\varphi = \varphi_0$ for $Pr = 0.02$, $Re = 2130$ and $m = 2$. The contact angles are $\alpha = 30^\circ$ (*a*), $\alpha = 70^\circ$ (*b*), and $\alpha = 120^\circ$ (*c*).

From the foregoing, the efficiency of the two instability mechanisms depends on the contact angle in an opposing manner. At intermediate values of $\alpha$ both mechanisms are operative leading to an optimum (minimum) critical Reynolds number $Re_c$ (figure 10).

5.1.3. *Gravity effects*

Gravity affects the flow in a liquid bridge in two ways. First, the hydrostatic pressure (measured by $Bo$) removes the mirror symmetry of the free surface with respect to $z = 0$ and, secondly, buoyancy bulk forces arise for $Gr \neq 0$.

While the ratio $Gr/Bo$ depends on both experimental control parameters $d$ and $\Delta T$, the ratio $Bd/Bo = Gr/BoRe = \beta\sigma_0/\gamma$ depends only on the material parameters

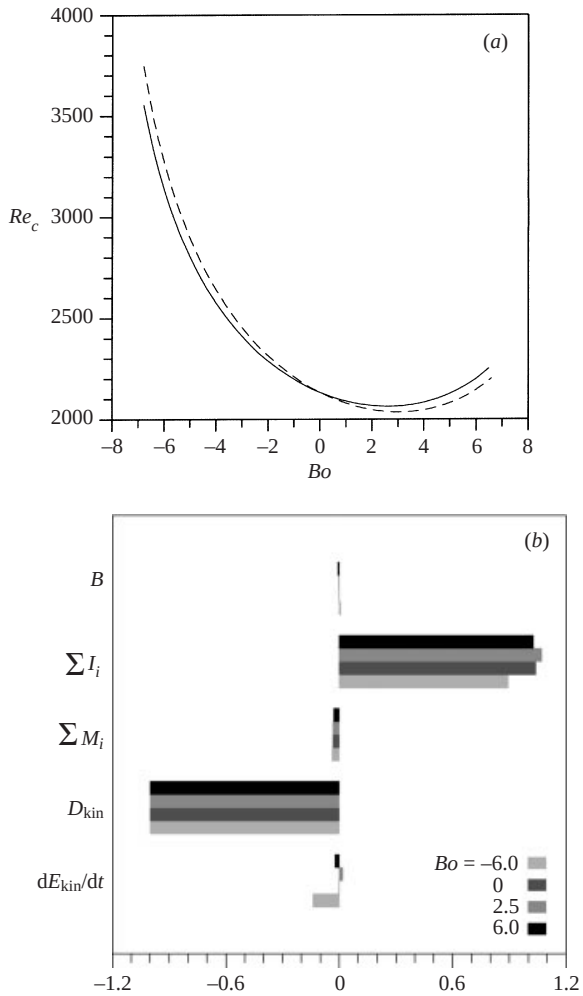


FIGURE 12. $Pr = 0.02$: (*a*) Critical Reynolds number as function of the static Bond number $Bo$ (dashed: $Bd = 0$, solid: $Bd/Bo = 0.27$) for $\mathscr{V} = 1$. The remaining parameters are $m = 2$ and $\Gamma = 1$. (*b*) Kinetic energy budget of the most dangerous modes for constant $Re = Re_c(Gr = Bo = 0) = 2130$ and different Bond numbers $Bo$.

($Bd = Gr/Re$ is the dynamic Bond number). Therefore, we consider in this section a constant ratio $Bd/Bo = 0.27$ valid for liquid tin.†

The signs of $Gr$ and $Bo$ distinguish heating from above ($Gr, Bo > 0$), i.e. the acceleration due to gravity is directed parallel to the thermocapillary forces, from heating from below ($Gr, Bo < 0$). In the subsequent figures the hot disk will always be in the upper part. Hence, for $Gr, Bo < 0$ the acceleration due to gravity is directed upwards. For small dynamic Bond numbers thermocapillary forces dominate buoyant ones. Under this condition the basic flow is unique (Wanschura, Kuhlmann & Rath 1997).

First, we consider $\mathscr{V} = 1$. In figure 12(*a*) the critical Reynolds number is given as

† The material parameters of liquid tin at $T = 505$ K are $\nu = 3.97 \times 10^{-7}$ m$^2$ s$^{-1}$, $\kappa = 1.76 \times 10^{-5}$ m$^2$ s$^{-1}$, $\sigma_0 = 0.62$ kg s$^{-2}$, $\gamma = 2.1 \times 10^{-4}$ kg s$^{-2}$ K, and $\beta = 9.0 \times 10^{-5}$ K$^{-1}$. This leads to $Pr \approx 0.02$ and $Bd/Bo \approx 0.27$.

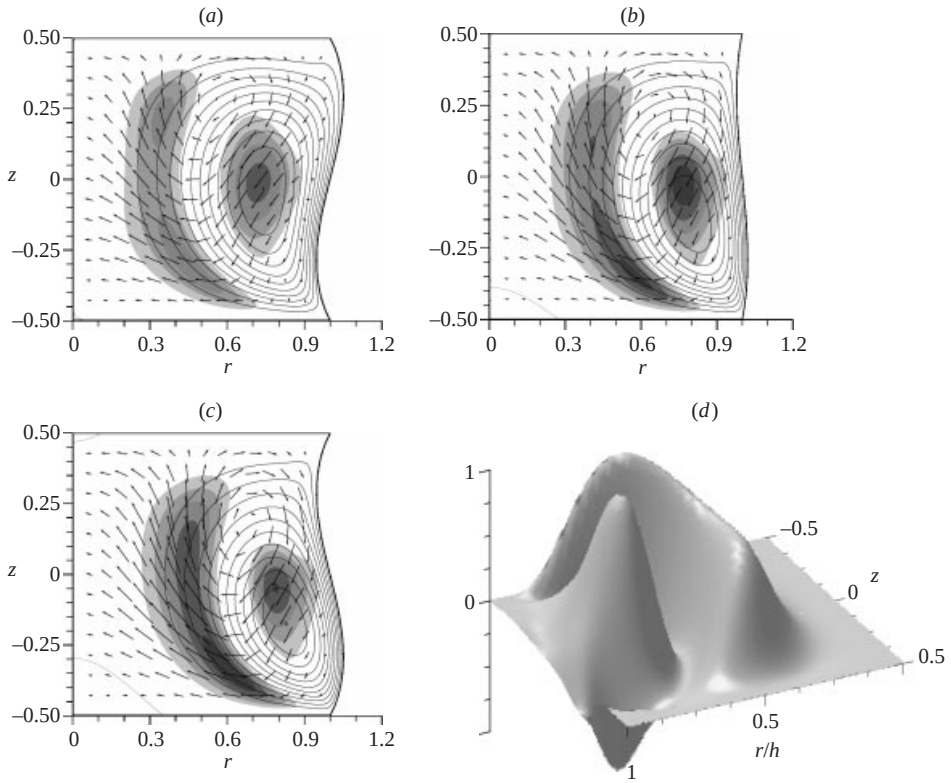


FIGURE 13. The inertial instability mechanism for $Pr = 0.02$, $Bd/Bo = 0.27$, $Re = 2130$, and $m = 2$ for $Bo = -6$ ($a$), $Bo = -2.5$ ($b$) and $Bo = 6$ ($c$). Representation of the basic flow, the most dangerous mode, and the kinetic production as in figure 11. ($d$) The distribution of the local production $\int \sum i_i \, r \mathrm{d}\varphi$ for $Bo = -2.5$ ($b$).

a function of the static Bond number for $Bd/Bo = 0.27$ (solid line). Over the whole range shown the critical azimuthal wavenumber is $m_c = 2$. At $Bo = Bo^\star \approx 2.5$ the stability boundary exhibits a minimum of $Re_c^{\min}(Bo) = Re_c(Bo^\star) \approx 2060$. Hence, the most unstable situation is obtained for a moderate heating from above. To distinguish between the influence of surface deformation and buoyancy effects the dashed curve shows the result when buoyancy is artificially neglected ($Bd = 0$). Since the two curves do not differ much we conclude that the major factor determining the change of stability is the deformation effect. For heating from above ($Bo > 0$), buoyancy leads to an increase in the stability boundary, while for heating from below ($Bo < 0$) the stability boundary is decreased. This is consistent with the result for straight cylindrical liquid bridges (Wanschura *et al.* 1997).

The kinetic energy balances of the most dangerous perturbations (i.e. those with the largest growth rate) for $Re = 2130$ shown in figure 12($b$) confirm that buoyant production $B$ and Marangoni work $M_{r,\varphi,z}$ are negligible compared to the production $\sum I_i$.

The critical Reynolds number is mainly influenced by the free-surface-shape-induced modifications of the velocity field. For $Bo = Bo^\star$, the centre of the basic vortex is located slightly in the colder half of the liquid bridge and suffers a significant straining (figure 13$c, d$). When $Bo$ increases from $Bo^\star$ the centre of the basic vortex shifts towards the convex part of the free surface in the lower half of the

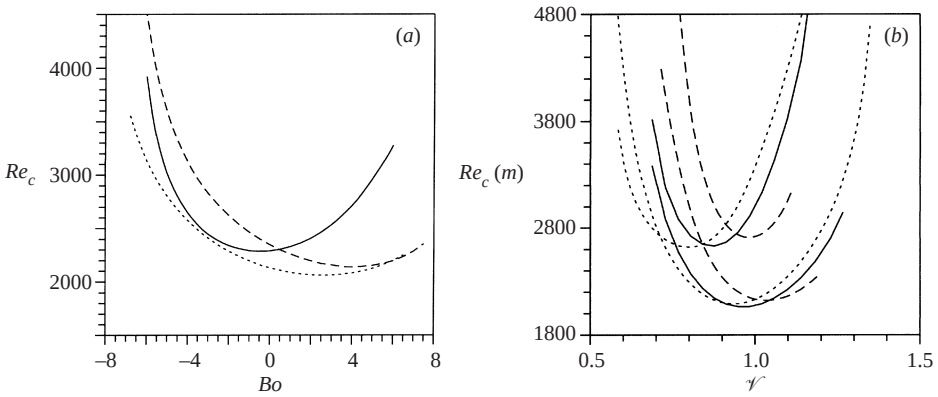


FIGURE 14. $Pr = 0.02$ and $\Gamma = 1$. ($a$) Critical Reynolds number $Re_c$ as function of the static Bond number $Bo$ for $\mathscr{V} = 0.8$ (full line), $\mathscr{V} = 1$ (dotted line) and $\mathscr{V} = 1.1$ (dashed line) and for $Bd/Bo = 0.27$. The critical azimuthal wavenumber is $m = 2$ in all cases. ($b$) $Re_c(m)$ as a function of the relative volume $\mathscr{V}$ for $Bo = 1.7$ (full lines) and $Bo = 5.3$ (dashed lines) with $Bd/Bo = 0.27$. For comparison, the neutral curves $Re(\mathscr{V}, m = 1, 2)$ for $Bo = Bd = 0$ are added (dotted lines). The upper set of curves corresponds to $m = 1$ and, the lower set to $m = 2$.

bridge (figure 13$c$). Thereby, the cross-stream gradient of $\boldsymbol{U}_0$ is increased in the jet which originates from the cold corner, promoting the centrifugal instability process (figure 13$c$). Owing to the convex shape of the free surface, however, the strain on the vortex centre is less. This effect overcompensates the energy gain through the centrifugal process, resulting in a net stabilization for large $Bo$. For negative Bond numbers both the straining and the centrifugal process are weakened, because the vortex centre moves to the mid-plane $z = 0$ (figure 13$a$).

For volumes fractions $\mathscr{V} \neq 1$ a similar behaviour is found. Figure 14($a$) shows the critical Reynolds numbers as a function of $Bo$ with $Bd/Bo = 0.27$ for $\mathscr{V} = 0.8$, $\mathscr{V} = 1$ and $\mathscr{V} = 1.1$. The location of the minimum critical Reynolds number $Re_c^{\min}(Bo)$ is determined by the relative efficiency of the two instability mechanisms discussed above. From § 5.1.2 for $Bo = 0$, the production due to centrifugal effects increases with increasing volume $\mathscr{V}$ and the production due to strain decreases with $\mathscr{V}$. This also applies to constant non-zero Bond numbers $Bo \neq 0$. At $\mathscr{V} = 1.1$ the instability mechanism is dominated by centrifugal effects and the minimum of the critical curve $Re_c(Bo)$ is shifted to higher Bond numbers. As can be concluded from figure 14($a$) centrifugal effects are less important for $\mathscr{V} = 0.8$ and the minimum of $Re_c(Bo)$ occurs at $Bo \approx -0.5$ at which the straining effect is large.

The relative importance of centrifugal and straining effects also determines the neutral curves $Re_c(\mathscr{V}, m)$ for different non-zero Bond numbers as shown in figure 14($b$). For $Bo = 1.7$ and $Bo = 5.3$ the critical wavenumber is $m_c = 2$ over the entire range of $\mathscr{V}$, unlike $Bo = 0$ for which also $m = 1$ may become critical. When $Bo$ increases the minima of $Re_c(\mathscr{V})$ are shifted towards larger values of $\mathscr{V}$. This can be understood in terms of the increasing cold-corner contact angle $\alpha_c$ and the more convex surface shape when $\mathscr{V}$ is increased. These conditions lead to an increased centrifugal destabilization and a reduced strain on the vortex core.

In summary, gravity modifies the linear stability boundary ($Re_c$) in low-Prandtl-number half-zones mainly via hydrostatic surface deformations. Buoyancy is of much lesser importance. For $\Gamma = 1$, considered here, gravity promotes the selection of $m = 2$ as the critical wavenumber.

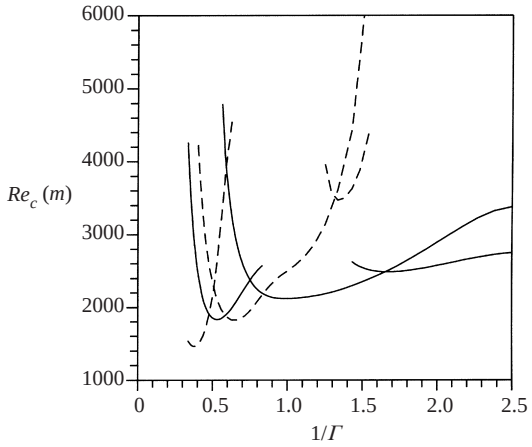


FIGURE 15. Curves of neutral stability for $Pr = 0.02$ and $Bo = Gr = 0$ as function of the inverse aspect ratio $1/\Gamma$. The full lines indicate $\alpha = 70°$, the dashed ones $\alpha = 115°$. The azimuthal wavenumbers of the neutral curves are $m = 1, 2, 3$ in increasing order from left to right, i.e. for decreasing aspect ratio.

#### 5.1.4. *Influence of the aspect ratio*

The dependence of the neutral Reynolds numbers on the inverse aspect ratio is shown in figure 15 for a concave ($\alpha = 70°$) and a convex ($\alpha = 115°$) liquid bridge under zero-gravity conditions. For low-Prandtl-number cylindrical liquid bridges the neutral curves for each wavenumber $m$ have a minimum at aspect ratios approximately satisfying $m \simeq 2/\Gamma$ (Wanschura *et al.* 1995). We find that the instability mechanisms do not change in the range of $\Gamma$ investigated, neither for slender ($\alpha = 70°$) nor for fat bridges ($\alpha = 115°$). Also, the ordering with respect to $\Gamma$ of the minima of the neutral curves for each $m$ remains qualitatively unchanged. Merely, the minima of the neutral curves are slightly shifted with respect to $\Gamma$, particularly for $\alpha = 115°$. This shift of the neutral curves can be understood in terms of an *effective aspect ratio*: the scaled neck radius for concave shapes is smaller than unity and varies from $h_{\min}(\alpha = 70°, \Gamma = 0.4) = 0.92$ to $h_{\min}(\alpha = 70°, \Gamma = 3) = 0.88$, while a convex shape represents a smaller effective aspect ratio, because the scaled maximum radius is larger than unity and varies from $h_{\max}(\alpha = 115°, \Gamma = 0.65) = 1.10$ to $h_{\max}(\alpha = 115°, \Gamma = 3) = 1.14$.

### 5.2. *High Prandtl numbers*

For high Prandtl numbers ($Pr \gtrsim 1$) the two-dimensional flow in cylindrical liquid bridges becomes linearly unstable to a pair of travelling hydrothermal waves (Wanschura *et al.* 1995; Leypoldt, Kuhlmann & Rath 2000). For waves, the imaginary part of the growth rate $\mu$ is non-zero at criticality and the amplitudes of the normal modes (3.7) are complex. This doubles the memory demand, because complex arithmetic is necessary. In addition, high gradients of the temperature and axial velocity of the basic state near the hot and cold corners must be resolved. Convergence tests of the critical Reynolds number by using different grids indicate reliable results for $Pr = 4$ in the range $30° \leqslant \alpha \leqslant 130°$ (table 7). A linear dependence of the critical Reynolds numbers on the squared mean grid spacing $\bar{\Delta}^2$ is obtained on the finest grids used, enabling Richardson extrapolation.

The only linear stability data available to date are those of Chen *et al.* (1999). A comparison with their results is shown in table 8. In most cases the neutral Reynolds

| $N_\xi \times N_\eta$ | $\alpha = 30°$ $m = 1$ | $\alpha = 50°$ $m = 1$ | $\alpha = 50°$ $m = 2$ | $\alpha = 90°$ $m = 2$ | $\alpha = 110°$ $m = 2$ | $\alpha = 130°$ $m = 2$ |
|---|---|---|---|---|---|---|
| $48 \times 71$ | 739 | 1150 | 1443 | 906 | 713 | 645 |
| $65 \times 95$ | 1035 | 1238 | 1431 | 952 | 754 | 715 |
| $71 \times 105$ | 1116 | 1277 | 1433 | 963 | 770 | 733 |
| $81 \times 119$ | 1174 | 1318 | 1435 | 972 | 785 | 749 |
| $93 \times 137$ | 1213 | 1359 | 1438 | 981 | 796 | 762 |
| Extrapolated | 1350 | 1470 | 1445 | 1010 | 840 | 800 |
| Wanschura *et al.* (1995) | | | | 1049 | | |
| Leypoldt (2000) | | | | | | 790 |

TABLE 7. Neutral Reynolds numbers $Re_c(m)$ for $Pr = 4$ and several contact angles obtained on different grids ($\Gamma = 1$, $Bo = Gr = 0$). The result from Leypoldt (private communication) was obtained by numerical simulation.

| $\Gamma$ | $\mathscr{V}$ | Present | Chen *et al.* (1999) |
|---|---|---|---|
| 1.4 | 0.8 | 2550 | 2590 |
| 1.4 | 1.0 | 2490 (2340) | 2590 |
| 1.4 | 1.2 | 4820 (1860) | 3350 |
| 1.6 | 0.8 | 2490 | 2560 |
| 1.6 | 1.0 | 2140 | 2240 |
| 1.6 | 1.2 | 2360 (2050) | 3400 |

TABLE 8. Neutral Reynolds numbers $Re_c(m = 1)$ for $Pr = 1$ and different volume fraction $\mathscr{V}$ and aspect ratio $\Gamma$. ($Bo = Gr = 0$). The numbers in parentheses are values of $Re_c(m = 2)$.

numbers for $Pr = 1$ and $m = 1$ are in good agreement. However, for larger volumes the deviations become significant and we even found a different critical wavenumber $m_c = 2$, in some cases. These differences are presumably due to the fully spectral method (Chebyshev collocation) used by Chen *et al.* (1999) in conjunction with a severe mode truncation and a strong smoothing ($s = 0.1$) which was copied from Wanschura *et al.* (1995) and which extended over a length which was 50 times larger than the present value ($s = 0.002$).

#### 5.2.1. *General instability mechanisms*

The instability mechanism in thermocapillary flows of high-Prandtl-number fluids when the temperature gradient is parallel to the interface was first explained by Smith & Davis (1983), who coined the term *hydrothermal wave* for the instability modes. The analysis has been extended to cylindrical liquid bridges by Wanschura *et al.* (1995) who found essentially the same destabilization process leading to a pair of azimuthally propagating hydrothermal waves. In these waves weak oscillating flows produce large temperature fluctuations by convective transport of the basic temperature field $T_0$. The temperature fluctuations, in turn, drive the flow field via the (mainly azimuthal) thermocapillary effect. Hence, the thermal energy balance (3.9*b*) is crucial for an understanding of the instability process (Smith & Davis 1983; Wanschura *et al.* 1995).

In our decomposition, there are two transport terms which contribute to the production of thermal energy: $j_1 \sim \theta u \partial_r T_0$ and $j_2 \sim \theta w \partial_z T_0$. For $Pr = 4$, and also for all larger Prandtl numbers, an extended region of high radial temperature gradients

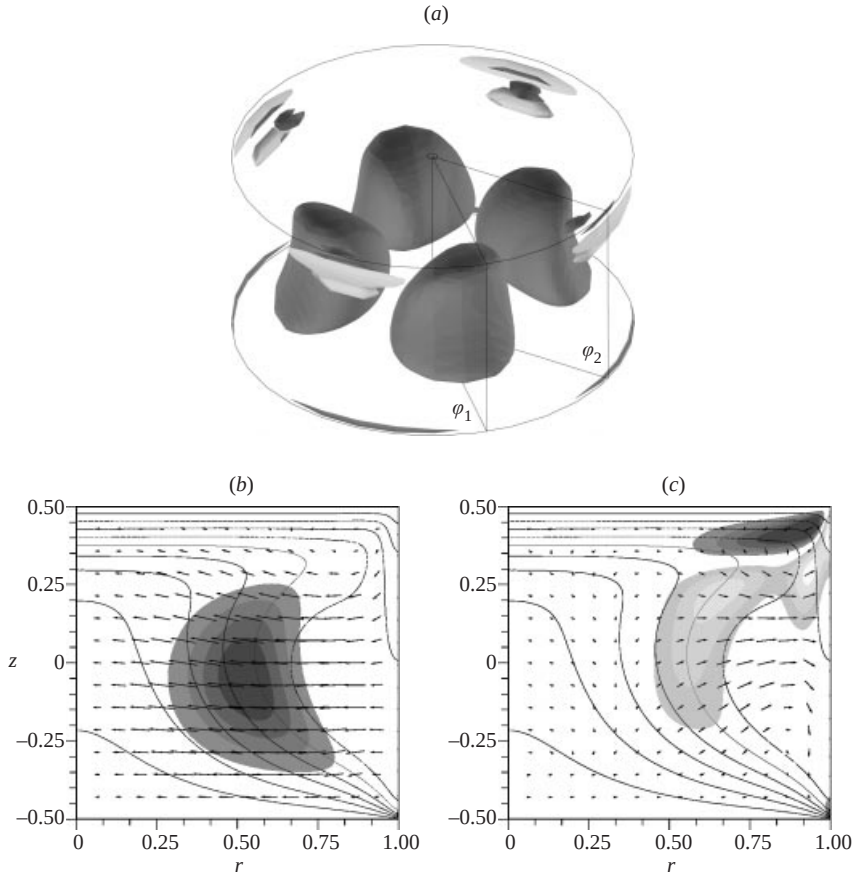


FIGURE 16. Critical mode for $Pr = 4$, $\Gamma = 1$, $Bo = Gr = 0$, and $\alpha = 90^\circ$ ($m_c = 2$). (*a*) Isosurfaces of negative (light grey) and positive (dark grey) values of $j_1$ and $j_2$. (*b*, *c*) Isolines of the basic-state temperature and perturbation velocity field together with shaded regions of negative (light grey) and positive (dark grey) extrema of $j_1 + j_2$ at $\varphi = \varphi_1$ (*b*) and at $\varphi = \varphi_2$ (*c*).

$\partial_r T_0$ exists in the bulk near $(r, z) = (0.5h, 0)$ (cf. figure 3). In this region $j_1$ takes its maximum value. High axial gradients $\partial_z T_0$, on the other hand, occur near the hot wall and the cold corner. The corner regions potentially promote thermal energy production by axial transport of basic-state energy as expressed by $j_2$.

For a cylindrical liquid bridge with $\alpha = 90^\circ$, $Pr = 4$, $\Gamma = 1$, and $Bo = Gr = 0$, $J_1$ almost perfectly balances the thermal dissipation (not shown). The distribution of the local production rates $j_1$ and $j_2$ of the critical mode is shown in figure 16(*a*), where the extended regions of energy gain in the bulk correspond to $j_1$. If we define the instantaneous orientation of the wave $\varphi_1$ by $j_1(r, \varphi_1, 0) = \max_{r,\varphi}\{j_1(r, \varphi, 0)\}$ and $u(r, \varphi_1, 0) < 0$, then the secondary regions of production near the hot and cold corners are found near $\varphi_2 = \varphi_1 + \pi/2m$. The perturbation flow in the plane $\varphi_1$ (figure 16*b*) is mainly radial, acting on the radial gradients of $T_0$. This explains the major production term $J_1$. In the plane $\varphi_2$ the perturbation flow consists of eddies in the hot and cold corners (figure 16*c*) which act on the basic-state temperature gradients, giving rise to minor positive and negative contributions to $J_1$ and $J_2$ near the hot corner and to a sharp negative peak of $j_2$ near the cold corner.

The structure of the critical mode and the production terms does not change

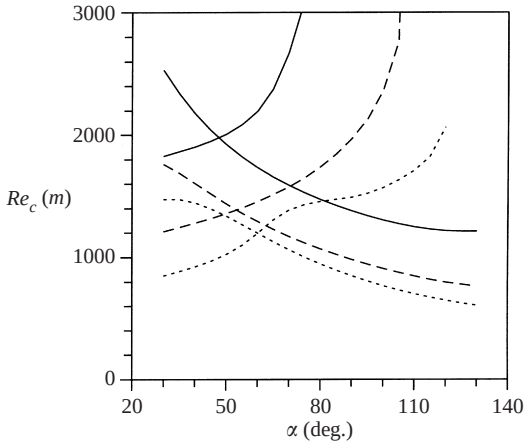


FIGURE 17. Curves of neutral stability $Re_c(m)$ for high Prandtl numbers as functions of the contact angle $\alpha$. $Pr = 2$ (—), $Pr = 4$ (– –), $Pr = 7$ (- - -). The intersections locate the change of the critical wavenumber $m_c$. The curves with a positive slope correspond to $m = 1$ while the monotonically decreasing curves corresponds to $m = 2$.

| $Pr$ | $\alpha^{\max}$ (deg.) | $Re_c(\alpha^{\max})$ | $Ma_c(\alpha^{\max})$ |
|---|---|---|---|
| 2 | 48 | 1950 | 3900 |
| 4 | 53 | 1390 | 5560 |
| 7 | 60 | 1200 | 8400 |

TABLE 9. Maximum values of $Re_c(\alpha)$ and $Ma_c(\alpha)$ at $\alpha = \alpha^{\max}$ for $Pr = 2$, 4, 7, and $\Gamma = 1$, $Bo = Gr = 0$.

qualitatively for the parameters investigated in this section, when the free-surface shape is varied. It is the relative magnitude of the bulk production via $j_1$ with respect to the production near the corners which affects the critical Reynolds number.

5.2.2. *Volume-of-fluid effects*

To investigate the effect of the volume fraction $\mathscr{V}$ on the linear stability we first neglect gravity ($Bo = Gr = 0$). Figure 17 shows the neutral Reynolds numbers as functions of $\alpha$ for unit aspect ratio and for $Pr = 2$, 4, and 7. For all values of $Pr$, the critical wavenumber at small contact angles is $m_c = 1$. The corresponding neutral curves $Re_c(m = 1)$ increase with $\alpha$. On the other hand, the neutral curves for $m = 2$ which are critical at large contact angles are monotonically decreasing. At the intersection point of the two neutral curves for $m = 1$ and $m = 2$ at a given $Pr$, the critical Reynolds number has a local maximum. These codimension-2 points occur for $\alpha = 48°$ ($Pr = 2$), $\alpha = 53°$ ($Pr = 4$), and $\alpha = 60°$ ($Pr = 7$) (cf. table 9). The respective maximum critical Reynolds number decreases with increasing Prandtl number.

The change of the critical wavenumber from $m_c = 2$ to $m_c = 1$, when the contact angle $\alpha$ is decreased, can be understood by considering the primary energy production term $j_1 \sim Ma\theta u\partial_r T_0$ at $z = 0$. It is observed that the maximum of $\partial_r T_0(r, z = 0)$ moves closer to the axis $r = 0$ for decreasing $\alpha$ (figure 18*a*). Accordingly, the regions of amplification due to $j_1$ are slightly displaced towards the axis (figure 18*b*). Since the perturbation velocity for modes with $m = 1$ need not vanish on the axis $r = 0$

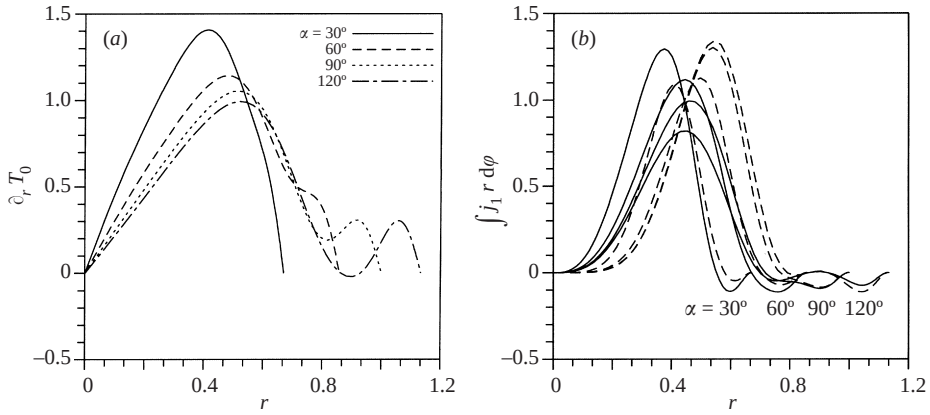


FIGURE 18. At mid-plane $z = 0$ and as functions of $r$. ($a$) Radial gradient of the basic-state temperature. The contact angle is indicated by labels ($\alpha = 30°, 60°, 90°, 120°$). ($b$) Local energy production $\int j_1\, r\mathrm{d}\varphi$ for $m = 1$ (solid) and $m = 2$ (dashed). The remaining parameters for both plots are $Pr = 4$, $\Gamma = 1$, $Bo = Gr = 0$, and $Re = 1000$.

whereas higher modes must vanish there (B 4$b$), ($m = 1$)-modes are more effective in extracting energy from the basic temperature field of slender liquid bridges by the process $j_1$ than modes with $m > 1$. For convex shapes, on the other hand, the region of maximum $\partial_r T_0(r, z = 0)$ arises at a larger distance from the axis and the modes with $m = 2$ are more efficient regarding the $J_1$-mechanism than those with $m = 1$ (figure 18$b$).

The relative importance of the energy transfer processes in the bulk and near the corners can be assessed from figure 19. For two reasons the corner regions become more important for the instability when $\alpha$ increases. First, the axial gradients of $T_0$ near the corners are enhanced for large $\alpha$. This is the result of the adiabatic boundary condition on the free surface. Second, large contact angles facilitate the penetration of perturbation eddies into the corners. The positive peak of $j_2$ near the cold corner increases rapidly for large $\alpha$ due to the large axial basic temperature gradient, but its integral contribution remains small. In particular for modes with $m = 1$, it is the loss of energy (negative production) near the hot corner that increases with $\alpha$, as does the critical Reynolds number $Re_c(m = 1)$ for convex half-zones.

### 5.2.3. *The effect of gravity*

For an investigation of gravity effects we consider the same ratio of the dynamic to the static Bond number, $Bd/Bo = 0.27$, as for small Prandtl numbers (§ 5.1.3). This is reasonable with respect to the material parameters of high-Prandtl-number fluids, like acetone ($Pr = 4.4$, $Bd/Bo = 0.29$) or methanol ($Pr = 6.9$, $Bd/Bo = 0.31$) (sodium nitrate used by Velten *et al.* (1991), has $Pr = 7$ and $Bd/Bo = 0.08$), and it facilitates a comparison between the two cases.

In the absence of surface deformations ($Bo = 0$) and for dominating thermocapillary flow, Wanschura *et al.* (1997) has shown that buoyancy ($|Gr| \neq 0$) is nearly always stabilizing, except for small positive values of $Gr$. The same holds if surface deformations are taken into account ($Bo \neq 0$). To discuss the dependence on $Bo$, the critical Reynolds number for constant volume $\mathscr{V} = 1$ is shown in figure 20($a$) as a function of $Bo$. In the absence of buoyancy ($Bd = 0$) the critical Reynolds number depends nearly linearly on the Bond number in the range considered. The basic flow is stabilized for $Bo > 0$, whereas it is destabilized for $Bo < 0$. If, however, buoyancy

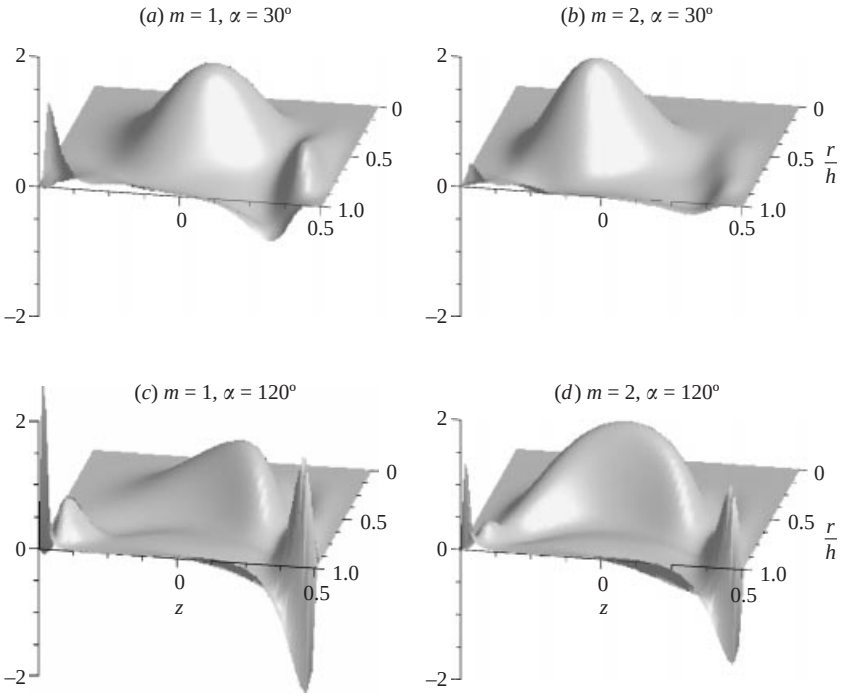


FIGURE 19. Local thermal production rates $\int (j_1 + j_2)\, r \mathrm{d}\varphi$ of the most dangerous perturbation modes with $m = 1$ and $m = 2$ of the flow in a concave ($\alpha = 30°$) and a convex ($\alpha = 120°$) half-zone for $Re = 1000$. Remaining parameters: $Pr = 4$, $\Gamma = 1$, $Bo = Gr = 0$.

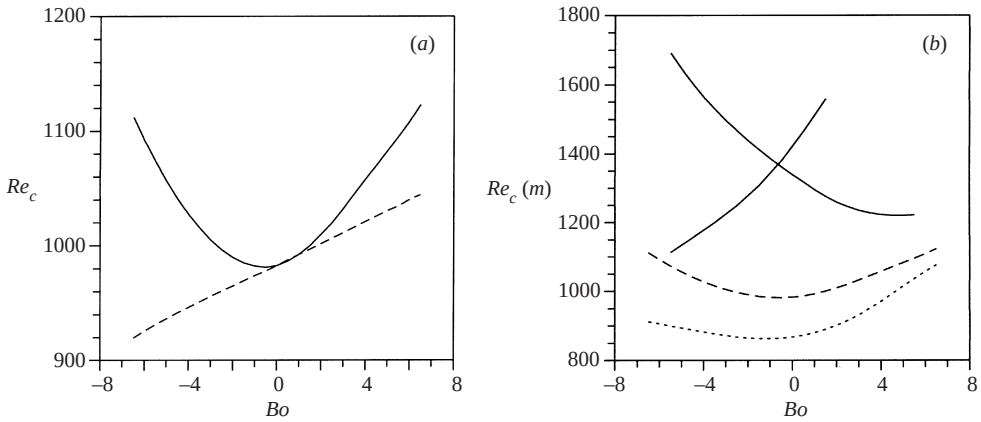


FIGURE 20. $Pr = 4$. (*a*) Critical Reynolds number as function of the static Bond number $Bo$ for $\mathscr{V} = 1$ (dashed: $Bd = 0$, solid: $Bd/Bo = 0.27$), $m_c = 2$. (*b*) Critical Reynolds numbers $Re_c(m)$ as function of $Bo$ for $Bd/Bo = 0.27$ and $\mathscr{V} = 1.1$ (dotted, $m_c = 2$), $\mathscr{V} = 1$ (dashed, $m_c = 2$), and $\mathscr{V} = 0.8$ (solid, positive slope: $m = 1$, negative slope: $m = 2$).

is accounted for ($Bd/Bo = 0.27$) the critical Reynolds number $Re_c(Bo)$ exhibits a clear minimum near $Bo = 0$. For heating from above ($Bo > 0$) the flow stabilization due to $Bo$ is enhanced and for heating from below ($Bo < 0$) the stabilizing action of buoyancy overcomes the destabilization due to the shape effect, except for very small negative $Bo$, where $Re_c$ takes its minimum value. We conclude that buoyancy forces

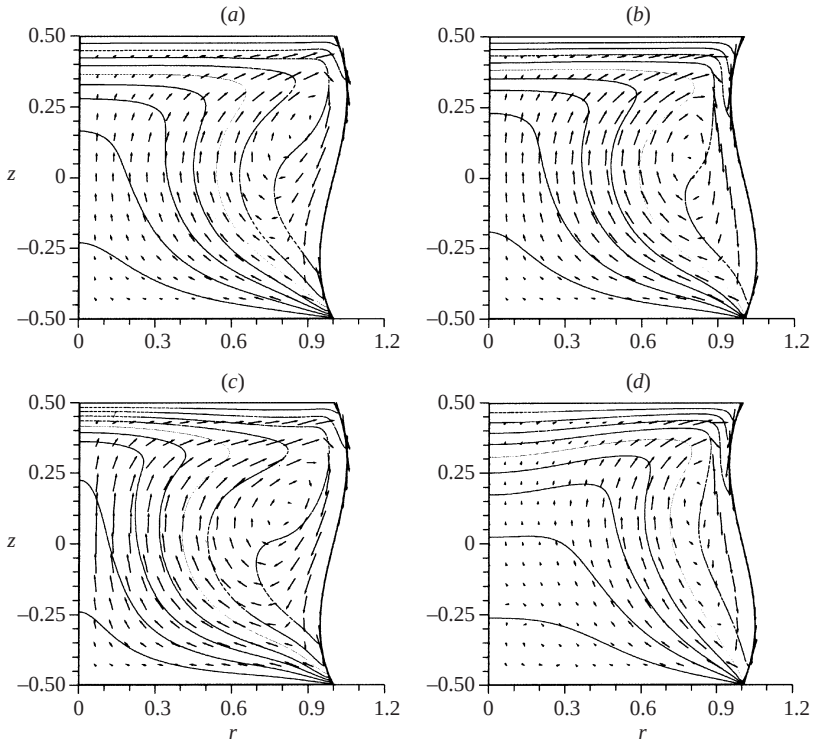


FIGURE 21. $Pr = 4$: Isotherms (lines) and velocity field (arrows) of the basic flow. $(a, c)$: Heating from below ($Bo = -6$), $Bd = 0$ $(a)$ and $Bd/Bo = -0.27$ $(c)$, respectively. $(b, d)$: Heating from above ($Bo = 6$), $Bd = 0$ $(b)$ and $Bd/Bo = 0.27$ $(d)$, respectively. The remaining parameters are $\mathscr{V} = 1$ and $Re = 1000$.

play the dominant role for the critical Reynolds number whereas hydrostatic surface deformations are of lesser importance when $Bd/Bo = 0.27$.

Figure 21 shows the effect of gravity on the basic flow and the temperature field. As a result of the deformation effect for $Bo \neq 0$ the centre of the basic toroidal vortex is displaced from its position at $Bo = 0$ towards the free surface where it bulges outward (convex part of the free surface, see figure 21$a, b$). Since the temperature field depends sensitively on the velocity field for high Prandtl numbers, this displacement causes a modification of the gradient $\partial_r T_0$ in the bulk near $z = 0$: As seen from figure 22$(a)$, $\partial_r T_0$ is slightly reduced in magnitude if $Bo$ increases from zero. This explains the weak stabilization due to the shape effect (see figure 20$a$). It has been shown before that buoyancy effects are stronger than deformation effects for $Bd/Bo = 0.27$ (compare also figure 22$b$). This can also be seen from figure 21$(c, d)$ in which the return flow near the axis is strongly enhanced for heating from below as compared to figure 21$(a, b)$, while it is reduced near the axis, due to the stable thermal stratification when the heating is from above. In both cases, however, $\partial_r T_0$ is reduced in the region around $r \approx 0.5$ such that the efficiency of the primary instability mechanism is reduced, which explains the minimum of $Re_c$ in figure 20$(a)$.

Critical curves $Re(Bo, Bd/Bo = 0.27)$ for several volume fractions are shown in figure 20$(b)$. The critical curve for an increased volume $\mathscr{V} = 1.1$ does not differ qualitatively from that for $\mathscr{V} = 1$. Merely, the threshold for $m_c = 2$ is reduced. However, when the volume is reduced a codimension-2 point appears near $Bo = 0$.

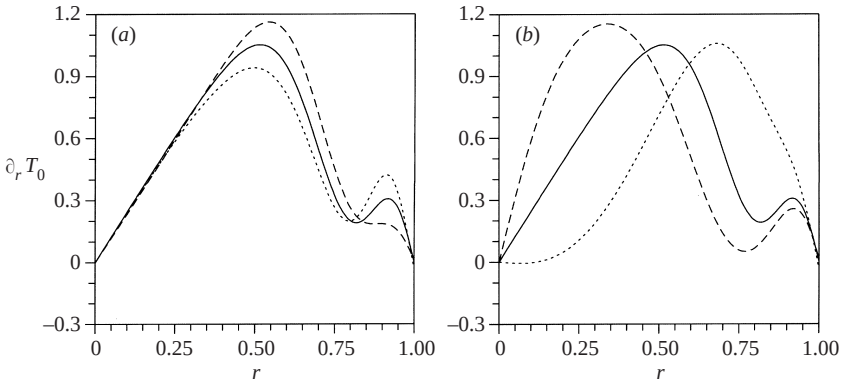


FIGURE 22. Radial gradients of the basic-state temperature at $z = 0$ shown for $Bo = 0$ (—), $Bo = -6$ (– –) and $Bo = 6$ (- - -). The dynamic Bond number is $Bd = 0$ ($a$) and $Bd/Bo = 0.27$ ($b$). The remaining parameters are $Pr = 4$, $\Gamma = 1$, and $Re = 1000$.

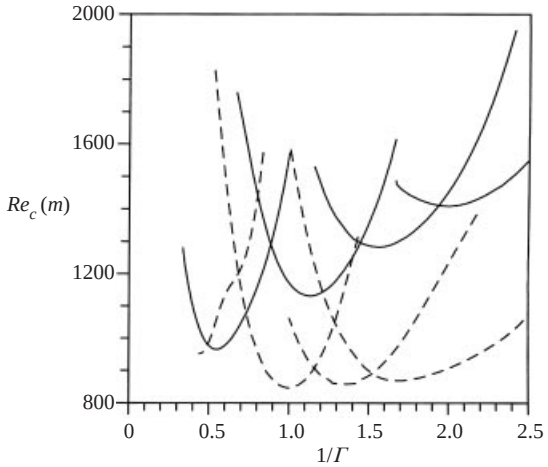


FIGURE 23. Curves of neutral stability for $Pr = 4$ and $Bo = Gr = 0$ as function of the inverse aspect ratio $1/\Gamma$. The full lines indicate $\alpha = 70°$ and the dashed ones $\alpha = 110°$. The azimuthal wavenumber of the neutral curves increases for each set of curves with decreasing aspect ratio from left to right as $m = 1, 2, 3, 4$.

For $\mathscr{V} = 0.8$, for example, the critical mode has $m = 1$ when $Bo \lesssim 0$ and $m = 2$ when $Bo \gtrsim 0$. From § 5.2.2 both a small volume fraction (small contact angle) and heating from below lead to high values of $\partial_r T_0$ at small radii. This situation promotes $m = 1$ modes. When the heating is from above and the contact angle is large, on the other hand, the highest radial temperature gradients arise at larger distance from the axis and the neutral mode for $m = 2$ is more effective.

In summary, the effect of buoyancy on the linear stability boundary is much stronger for $Bd/Bo = 0.27$ than the hydrostatic deformation effect. The efficiency of the instability mechanism is closely related to the high radial gradients of $T_0$ in the bulk, which are determined by the return flow of the thermocapillary vortex.

### 5.2.4. *Influence of the aspect ratio*

The dependence of the linear stability boundary on the aspect ratio is shown in figure 23 for $Pr = 4$ under zero gravity for $\alpha = 70°$ and $\alpha = 110°$. The ordering of

the neutral curves with respect to the wavenumber $m = 1, 2, 3, 4$ (the smaller $\Gamma$ the larger $m$) is in agreement with numerical results for cylindrical half-zones (Wanschura *et al.* 1995, $Bo = Gr = 0$) and experimental results for nearly cylindrical half-zones (Velten *et al.* 1991, $Bo \neq 0, Gr \neq 0$). Apart from changes in magnitude and shape, the neutral curves are found to shift towards larger values of $\Gamma^{-1}$ when the contact angle is decreased from $\alpha = 110°$. For $\alpha$ below 70° the shift of the neutral curves is even larger. The same qualitative behaviour applies to small Prandtl numbers (figure 15) and may likewise be interpreted as an increase of the *effective aspect ratio* when the contact angle is decreased. For $m \geqslant 2$, or $\Gamma \lesssim 1.4$ ($\Gamma^{-1} \gtrsim 0.71$), the neutral Reynolds numbers for $\alpha = 70°$ (full lines) are larger than those for $\alpha = 110°$ (dashed). This is in agreement with the general trend of the volume-of-fluid effect studied in § 5.2.2 for $\Gamma = 1$ (see figure 17 for $m = 2$). The difference between the critical Reynolds numbers $Re_c(\alpha = 70°)$ and $Re_c(\alpha = 110°)$ (envelopes of the neutral curves) increases with decreasing aspect ratio. Thus the volume-of-fluid effect on the critical Reynolds number becomes larger when the aspect ratio is decreased.

In the range of $\Gamma$ investigated the minima of the neutral curves approximately lie on a straight line ($\partial Re_c/\partial \Gamma^{-1} \approx$ const.). This dependence is not obvious and it is not known whether this applies to larger values of $\Gamma^{-1}$. We find that the smaller $\mathscr{V}$ the larger the slope (stabilization of the basic state). A plausible cause could be the higher viscous effects on the basic vortex and the neutral mode when the contact angle is small. Apparently this difference becomes more pronounced the larger $\Gamma^{-1}$.

## 6. Summary and conclusions

The linear stability of the two-dimensional steady flow in thermocapillary half-zones with static free-surface shape was investigated numerically. Results for the critical Reynolds numbers $Re_c$ were obtained as functions of the volume fraction $\mathscr{V}$, the Prandtl number $Pr$, the aspect ratio $\Gamma$, and the Bond number $Bo$. The effect of these parameters on the physical mechanisms has been highlighted by analysing the local energy production rates.

The dependence of the critical Reynolds number on the volume fraction is markedly different for small and large Prandtl numbers. For $\Gamma = 1$ and zero gravity, $Re_c(\mathscr{V})$ takes a minimum near a volume $\mathscr{V} \approx 0.9$ when the Prandtl number is small. For large Prandtl numbers a maximum is found for a volume near the cylindrical one. Whereas the minimum for small $Pr$ is smooth, the maximum for large $Pr$ is sharp and results from an intersection of two neutral curves with different wavenumbers ($m = 1$ and $m = 2$). We found that the higher the Prandtl number the sharper the local maximum of $Ma_c$ (cf. table 9). This result is in qualitative agreement with experiments of Masud *et al.* (1997) who used silicon oil with $Pr \approx 25$. They found a sharp variation and, in some cases, even a sudden change of the critical Reynolds number near $\alpha \approx 60°$ (corresponding to the extreme radius $h|_{z=0} = 0.86$). The region near the maximum is difficult to access in experiments with silicone oils of even higher Prandtl number, because the liquid bridge may break down (Hu *et al.* 1994). Moreover, the intersecting neutral branches may both have $m = 1$ at higher $Pr$ (Masud *et al.* 1997).

The increase in the critical azimuthal wavenumber $m_c$ with the inverse aspect ratio is well known. The rule of thumb $m_c\Gamma \approx 2$ applies to cylindrical half-zones of low and high Prandtl numbers (Preisser *et al.* 1983, Wanschura *et al.* 1995). Obviously, this trend also holds for non-cylindrical liquid bridges. To account for the shape effect, Lappa *et al.* (2001) suggested $m_c d/h|_{(z=0)} = 2$ for $Pr = 0.01$ and zero-gravity conditions. This behaviour is essentially confirmed here and extended to high $Pr$: on

an increase in the volume the neutral curves (for given $m$) as function of $\Gamma$ are shifted towards higher values of $\Gamma$, and vice versa. It should be pointed out, however, that the rule of Lappa *et al.* (2001) does not always strictly hold, it merely indicates the general trend.

The steady three-dimensional instability for small Prandtl numbers is essentially inertial. Previous explanations of the mechanism dwelt either on the self-induced strain in the basic vortex core caused by the toroidal vortex shape (Levenstam & Amberg 1995) or on the strain exerted by the thermocapillary shear stress (Wanschura *et al.* 1995). We found that, in addition, a centrifugal mechanism is important. Its relative magnitude explains the particular dependence of the critical Reynolds number on the shape of the liquid bridge. The centrifugal process arises near the cold corner where a jet transports the fluid from the free surface into the bulk. The curved streamlines and the deceleration near the cold wall promote centrifugal-flow effects. This phenomenon is very similar to the centrifugal instability in rectangular lid-driven cavities, recently discussed by Albensoeder *et al.* (2000): in cavities with a depth below the moving lid larger than 1.207 times the width of the cavity the critical mode is stationary. It receives its energy downstream from the jet emerging from the downstream end of the moving lid. This centrifugal mechanism is analogous to the process in low-Prandtl-number liquid bridges (compare figure 20 of Albensoeder *et al.* (2000) with figures 11*b* and 13*c*).

The instability of high-Prandtl-number flows, caused by hydrothermal waves (Wanschura *et al.* 1995), is not altered qualitatively by the shape of the zone. The prominent feature of these waves consists of pronounced internal temperature fluctuations which arise in the region of large (radial) basic-state temperature gradients. The onset of oscillations depends on the interface shape, because it affects the location and the magnitude of the energy-providing basic-state temperature gradients, mainly through the modified basic velocity fields, and particularly through the return flow in the bulk.

Since the character of the instabilities for small and large Prandtl numbers is very distinct, the effect of gravity on the critical onset is different, too. For small $Pr$ the basic temperature field practically decouples from the flow. Buoyancy effects are small due to the large thermal conductivity compared to convective heat transport. The basic vortex, and hence its stability, is mainly determined by the hydrostatic interface shape, i.e. by the hydrostatic pressure. On the other hand, for the same ratio of buoyant forces to hydrostatic forces ($Bd/Bo = 0.27$), the hydrothermal-wave instability mechanism for high Prandtl numbers is mainly affected by buoyancy rather than by the hydrostatic deformation of the free-surface shape: the basic temperature field is crucial for the instability mechanism, and it is susceptible to the buoyant convective transport.

A natural extension of the present work would be the inclusion of dynamic rather than static free-surface shapes which arise when the capillary number is non-zero, $Ca = \gamma \Delta T/\sigma_0 \neq 0$. Since dynamic free-surface deformations under typical experimental conditions are very small ($O$ (μm)) compared to the characteristic zone length ($O$(mm)) and because the instability mechanisms found are independent of the dynamic deformability of the free surface, it can be expected that dynamic deformations do not significantly alter the stability boundaries calculated for static shapes.

This work has been supported in part by DLR under grant number 50 WM 9443 and by NASDA in the framework of the *Marangoni-Convection-Modeling-Research* project. We are indebted to H. J. Rath for creating the academic environment

which has made this research possible. We also thank S. Yoda for his continued encouragement of this work.

## Appendix A. Basic-state equations in body-fitted coordinates

Using the mapping (3.5), equations (3.3) take the form

$$\left(\tilde{\nabla}^2 - \frac{\Gamma^2}{\xi^2}\right)\Omega_0 = \Gamma Re\left(h\partial_\eta \Psi_0\left(\partial_\xi - \frac{1}{\xi}\right) + h'(\partial_\xi + 1)\Psi_0\partial_\xi - h\tilde{\mathrm{D}}\Psi_0\partial_\eta\right)\Omega_0 + \Gamma h\frac{Gr}{Re}\partial_\xi T_0, \tag{A 1a}$$

$$\tilde{\nabla}^2 T_0 = \Gamma Ma((h\partial_\eta \Psi_0 + h'\Psi_0)\partial_\xi - h\tilde{\mathrm{D}}\Psi_0\partial_\eta)T_0, \tag{A 1b}$$

$$\left(\tilde{\nabla}^2 - \frac{\Gamma^2}{\xi^2}\right)\Psi_0 = h^2\Omega_0, \tag{A 1c}$$

where $\tilde{\nabla}^2$ and $\tilde{\mathrm{D}}$ are differential operators in the body-fitted coordinates:

$$\tilde{\nabla}^2 = (\Gamma^2 + (h'\xi)^2)\tilde{\mathrm{D}}\partial_\xi + (h'^2 - hh'')\xi\partial_\xi - 2hh'\xi\partial_{\xi\eta} + h^2\partial_{\eta\eta} \quad \text{and} \quad \tilde{\mathrm{D}} = \partial_\xi + \frac{1}{\xi}.$$

The transformed boundary conditions are

$$\Psi_0 = \partial_\eta \Psi_0 = 0, \quad T_0 = \pm\tfrac{1}{2} \quad \text{on} \quad \eta = \pm\tfrac{1}{2}, \tag{A 2a}$$

$$\Psi_0 = \Omega_0 = \partial_\xi T_0 = 0 \quad \text{on} \quad \xi = 0, \tag{A 2b}$$

and

$$\left.\begin{aligned} &\Psi_0 = 0 \\ &\Omega_0 = -2\frac{h''}{h\mathscr{N}^2}\partial_\xi \Psi_0 + \frac{1}{\mathscr{N}}\partial_\eta T_0 \\ &\frac{\Gamma\mathscr{N}}{h}\partial_\xi T_0 - \frac{h'}{\Gamma\mathscr{N}}\partial_\eta T_0 = 0 \end{aligned}\right\} \quad \text{on} \quad \xi = 1. \tag{A 2c}$$

The system (A 1) together with (A 2) is discretized by second-order finite differences on a non-equidistant grid with prescribed minimum spacing $\Delta^{\min}$ at the rigid walls and at the free surface. The grid is stretched geometrically by a factor $f$ towards the bulk up to a prescribed maximum grid spacing $\Delta^{\max}$.† For smaller values of $\xi$ or $\eta$, respectively, the grid is equidistant (see figure 2*b*). Accordingly, the grid points are

$$\xi_0 = 1, \quad \xi_{i+1} = \max\{0, \xi_i - \Delta_\xi^{\max}, \xi_i - f_\xi^i\Delta_\xi^{\min}\}, \quad i = 0, \ldots, N_\xi - 2,$$

$$\eta_0 = \pm\tfrac{1}{2}, \quad \eta_{j+1} = \pm\max\{0, |\eta_j| - \Delta_\eta^{\max}, |\eta_j| - f_\eta^j\Delta_\eta^{\min}\}, \quad j = 0, \ldots, \frac{1}{2}(N_\eta - 3).$$

Typical values are $\Delta^{\min} = 5\times10^{-5}\ldots10^{-3}$, $\Delta^{\max} = 10^{-2}\ldots5\times10^{-2}$, and $f = 1.05\ldots1.2$. The method allows a selective grid refinement near the cold and hot corners.

† In practice the precribed value of $\Delta^{\max}$ may be slightly modified to ensure an equidistant grid spacing in the bulk.

## Appendix B. Linear stability equations

For axisymmetric perturbations, $m = 0$, the solution of (3.6) is sought in the form of a stream function–vorticity formulation as for the basic state,

$$\mu Re h\hat{\omega} = \left(\tilde{\nabla}^2 - \frac{\Gamma^2}{\xi^2}\right)\hat{\omega} - \Gamma h\frac{Gr}{Re}\partial_\xi\hat{\theta} - \Gamma Re\left[\left(h\partial_\eta\Psi_0\left(\partial_\xi - \frac{1}{\xi}\right) + h'(\partial_\xi + 1)\Psi_0\partial_\xi - h\tilde{\mathrm{D}}\Psi_0\partial_\eta\right)\hat{\omega} + \left(h\partial_\eta\hat{\psi}\left(\partial_\xi - \frac{1}{\xi}\right) + h'(\partial_\xi + 1)\hat{\psi}\partial_\xi - h\tilde{\mathrm{D}}\hat{\psi}\partial_\eta\right)\Omega_0\right], \tag{B 1a}$$

$$\mu Mah\hat{\theta} = \tilde{\nabla}^2\hat{\theta} - \Gamma Ma[((h\partial_\eta\Psi_0 + h'\Psi_0)\partial_\xi - h\tilde{\mathrm{D}}\Psi_0\partial_\eta)\hat{\theta} + ((h\partial_\eta\hat{\psi} + h'\hat{\psi})\partial_\xi - h\tilde{\mathrm{D}}\hat{\psi}\partial_\eta)\Omega_0], \tag{B 1b}$$

$$0 = \left(\tilde{\nabla}^2 - \frac{\Gamma^2}{\xi^2}\right)\hat{\psi} - h^2\hat{\omega}, \tag{B 1c}$$

together with the boundary conditions

$$\hat{\psi} = \partial_\eta\hat{\psi} = \hat{\theta} = 0 \quad \text{on} \quad \eta = \pm\tfrac{1}{2}, \tag{B 2a}$$

$$\hat{\psi} = \hat{\omega} = \partial_\xi\hat{\theta} = 0 \quad \text{on} \quad \xi = 0, \tag{B 2b}$$

and

$$\left.\begin{aligned} \hat{\psi} &= 0 \\ \hat{\omega} &= -2\frac{h''}{h\mathscr{N}^2}\partial_\xi\hat{\psi} + \frac{1}{\mathscr{N}}\partial_\eta\hat{\theta} \\ 0 &= \frac{h'}{\Gamma\mathscr{N}}\partial_\eta\hat{\theta} - \frac{\Gamma\mathscr{N}}{h}\partial_\xi\hat{\theta} \end{aligned}\right\} \quad \text{on} \quad \xi = 1. \tag{B 2c}$$

For $m > 0$, the problem is formulated in primitive variables. The azimuthal velocity $\hat{v}$ is eliminated using the continuity equation and the azimuthal momentum equation is replaced by the Poisson equation for $\hat{p}$ as in Wanschura *et al.* (1995). The linear perturbation equations in mapped coordinates are then given by

$$\mu Re h\hat{u} = \frac{1}{h}\left[\tilde{\nabla}^2 + \frac{\Gamma^2}{\xi^2}\left(\hat{u} + 2\xi\partial_\xi\hat{u} - \frac{2\xi}{\Gamma}(h'\xi\partial_\xi\hat{w} - h\partial_\eta\hat{w})\right)\right] - \Gamma\partial_\xi\hat{p} - Re((\boldsymbol{U}_0\cdot\tilde{\boldsymbol{\nabla}})\hat{u} + (\hat{\boldsymbol{u}}\cdot\tilde{\boldsymbol{\nabla}})U_0), \tag{B 3a}$$

$$\mu Re h\hat{w} = (\xi h'\partial_\xi - h\partial_\eta)\hat{p} + \frac{1}{h}\tilde{\nabla}^2\hat{w} + \frac{Gr}{Re}h\hat{\theta} - Re((\boldsymbol{U}_0\cdot\tilde{\boldsymbol{\nabla}})\hat{w} + (\hat{\boldsymbol{u}}\cdot\tilde{\boldsymbol{\nabla}})W_0), \tag{B 3b}$$

$$\mu Mah\hat{\theta} = \frac{1}{h}\tilde{\nabla}^2\hat{\theta} - Ma((\boldsymbol{U}_0\cdot\tilde{\boldsymbol{\nabla}})\hat{\theta} + (\hat{\boldsymbol{u}}\cdot\tilde{\boldsymbol{\nabla}})T_0), \tag{B 3c}$$

$$0 = -\tilde{\nabla}^2\hat{p} + \frac{Gr}{Re}(h\partial_\eta\hat{\theta} - h'\xi\partial_\xi\hat{\theta}) - 2Re\tilde{\boldsymbol{\nabla}}\cdot((\hat{\boldsymbol{u}}\cdot\tilde{\boldsymbol{\nabla}})\boldsymbol{U}_0), \tag{B 3d}$$

where

$$\hat{\boldsymbol{u}}\cdot\tilde{\nabla}=(\Gamma\hat{u}-h'\xi\hat{w})\partial_\xi+h\hat{w}\partial_\eta,$$

$$\boldsymbol{U}_0\cdot\tilde{\nabla}=(\Gamma U_0-h'\xi W_0)\partial_\xi+hW_0\partial_\eta,$$

$$\begin{aligned}\tilde{\nabla}\cdot((\hat{\boldsymbol{u}}\cdot\tilde{\nabla})\boldsymbol{U}_0)=&\left[\left(\Gamma^2\left(\partial_\xi-\frac{1}{\xi}\right)U_0-\Gamma h'\xi\partial_\xi W_0\right)\partial_\xi+\Gamma h\partial_\xi W_0\partial_\eta\right]\hat{u}\\&+\left[\left(\Gamma(h\partial_\eta-h'\xi\partial_\xi+h')U_0-h'\xi^2\left(\frac{h}{h'\xi}\partial_\eta-\partial_\xi\right)W_0\right)\right.\\&\left.+\left(h(h\partial_\eta-h'\xi\partial_\xi)W_0-\frac{\Gamma}{\xi}hU_0\right)\partial_\eta\right]\hat{w}.\end{aligned}$$

The boundary conditions in body-fitted coordinates are

$$\hat{u}=\hat{w}=\partial_\eta\hat{w}=\hat{\theta}=0\quad\text{on}\quad\eta=\pm\tfrac{1}{2},\tag{B 4a}$$

$$\left.\begin{array}{ll}m=1: & \partial_\xi\hat{u}=\hat{w}=\hat{p}=\hat{\theta}=0\\ m\geqslant 1: & \hat{u}=\hat{w}=\hat{p}=\hat{\theta}=0\end{array}\right\}\quad\text{on}\quad\xi=0,\tag{B 4b}$$

and

$$\left.\begin{aligned}&\Gamma\hat{u}-h'\hat{w}=0,\\&\frac{\Gamma\mathscr{N}}{h}\partial_\xi\hat{\theta}-\frac{h'}{\Gamma\mathscr{N}}\partial_\eta\hat{\theta}=0,\\&\partial_\eta\hat{\theta}+\frac{\mathscr{N}}{h}(\Gamma\partial_\xi\hat{w}+h'\partial_\xi\hat{u})+\left(1-\frac{h'^2}{\Gamma^2}\right)\frac{h''}{\mathscr{N}\Gamma}\hat{w}-\mathscr{N}\frac{h'}{\Gamma}\partial_\eta\hat{w}=0,\\&\mathscr{N}m^2\hat{\theta}+(2\mathscr{N}^2-1)\partial_\xi\hat{u}+\mathscr{N}^2\partial_{\xi\xi}\hat{u}+\frac{h}{\Gamma}(2\mathscr{N}^2-1)\partial_{\xi\eta}\hat{w}\\&\quad-\frac{h'}{\Gamma}\left[\left(1+\frac{hh'}{\Gamma^2}\right)\hat{w}+\left(2\mathscr{N}^2-1-\frac{hh'}{\Gamma^2}\right)\partial_\xi\hat{w}+\frac{hh'}{\Gamma^2}\partial_\eta\hat{w}\right.\\&\quad\left.+\mathscr{N}^2\partial_{\xi\xi}\hat{w}+\frac{h^2}{\Gamma^2}\partial_{\eta\eta}\hat{w}+\frac{h}{\Gamma}\partial_{\xi\eta}\hat{u}\right]=0,\end{aligned}\right\}\quad\text{on}\quad\xi=1.\tag{B 4c}$$

## Appendix C. Terms arising in the energy balance of the normal modes

The viscous and thermal energy dissipation,

$$\begin{aligned}D_{\mathrm{kin}}&=\frac{1}{2}\int|\boldsymbol{S}|^2\,\mathrm{d}\mathscr{V}\\&=4\pi\int_{-1/2}^{1/2}\int_0^{h(z)}|(\nabla\times\hat{\boldsymbol{u}})|^2\,r\mathrm{d}\,r\,\mathrm{d}z+8\pi\int_{-1/2}^{1/2}[hh''|\hat{w}|^2-\Gamma^2|\hat{v}|^2]\,\mathrm{d}z,\end{aligned}\tag{C 1a}$$

$$D_{\mathrm{th}}=\int|\nabla\hat{\theta}|^2\,\mathrm{d}\mathscr{V}=4\pi\int_{-1/2}^{1/2}\int_0^{h(z)}|\nabla\hat{\theta}|^2\,r\mathrm{d}r\,\mathrm{d}z,\tag{C 1b}$$

are always positive. Since the neutral modes are only determined up to an arbitrary factor, all terms in the energy balance are normalized by the dissipation $D_{\mathrm{kin}}$ or $D_{\mathrm{th}}$,

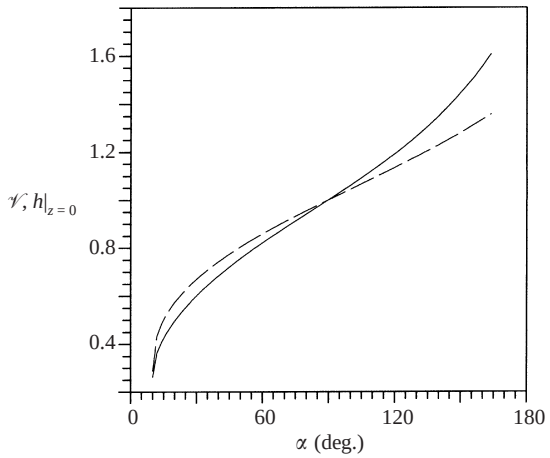


FIGURE 24. Dependence of the extreme radius $h|_{z=0}$ (– – –) and of the relative volume $\mathscr{V}$ (—) on the contact angle α.

| α (deg.) | $\mathscr{V}$ | $h\|_{z=0}$ | α (deg.) | $\mathscr{V}$ | $h\|_{z=0}$ | α (deg.) | $\mathscr{V}$ | $h\|_{z=0}$ |
|---|---|---|---|---|---|---|---|---|
| 20 | 0.496 | 0.573 | 64 | 0.846 | 0.879 | 108 | 1.110 | 1.080 |
| 24 | 0.542 | 0.617 | 68 | 0.870 | 0.899 | 112 | 1.136 | 1.098 |
| 28 | 0.583 | 0.654 | 72 | 0.894 | 0.918 | 116 | 1.163 | 1.115 |
| 32 | 0.620 | 0.686 | 76 | 0.918 | 0.936 | 120 | 1.190 | 1.134 |
| 36 | 0.653 | 0.716 | 80 | 0.941 | 0.955 | 124 | 1.219 | 1.152 |
| 40 | 0.685 | 0.743 | 84 | 0.965 | 0.973 | 128 | 1.249 | 1.171 |
| 44 | 0.715 | 0.769 | 88 | 0.988 | 0.991 | 132 | 1.280 | 1.189 |
| 48 | 0.743 | 0.793 | 92 | 1.012 | 1.009 | 136 | 1.313 | 1.209 |
| 52 | 0.770 | 0.816 | 96 | 1.036 | 1.027 | 140 | 1.348 | 1.228 |
| 56 | 0.796 | 0.838 | 100 | 1.060 | 1.044 | | | |
| 60 | 0.821 | 0.859 | 104 | 1.085 | 1.062 | | | |

TABLE 10. Dependence of the extreme radius $h|_{z=0}$ and of the volume fraction $\mathscr{V}$ on the contact angle α in numbers.

respectively, in order to enable a comparison of the mechanisms for different physical parameters. The production terms, numbered consecutively, become

$$I_1 + I_2 + I_3 + I_4 + I_5 = 4\pi \frac{Re}{D_{\mathrm{kin}}} \int \left[ -\frac{\Gamma}{r} |\hat{v}|^2 U_0 - \Gamma\, |\hat{u}|^2 \partial_r U_0 - \hat{u}^* \hat{w} \partial_z U_0 \right.$$
$$\left. -\Gamma\, \hat{w}^* \hat{u} \partial_r W_0 - |\hat{w}|^2 \partial_z W_0 \right] r \mathrm{d}r\, \mathrm{d}z, \qquad \text{(C 2)}$$

$$J_1 + J_2 = 4\pi \frac{Ma}{D_{\mathrm{th}}} \int [-\Gamma\, \hat{\theta}^* \hat{u} \partial_r T_0 - \hat{\theta}^* \hat{w} \partial_z T_0]\, r \mathrm{d}r\, \mathrm{d}z, \qquad \text{(C 3)}$$

where the asterisk denotes the complex conjugate. They describe the rate of change of the kinetic and thermal energy of the perturbation flow by convective transport (by the perturbations) of basic-state momentum and temperature, respectively. The particular decomposition into $I_1 \ldots I_5$ and $J_1$, $J_2$ is due to the cylindrical coordinate system employed.

The terms denoted $M_i$ represent the work per unit time done by Marangoni forces

on the fluid at the free surface,

$$M_r = \frac{4\pi\Gamma}{D_{\rm kin}} \int \hat{u}^* h \left[ \frac{h'}{\Gamma} (\Gamma \partial_r \hat{w} - \partial_z \hat{u}) \right] {\rm d}z, \tag{C 4a}$$

$$M_\varphi = \frac{4\pi\Gamma}{D_{\rm kin}} \int \hat{v}^* h \left[ \Gamma \left( \partial_r - \frac{1}{r} \right) \hat{v} - \frac{h'}{\Gamma} \partial_z \hat{v} \right] {\rm d}z, \tag{C 4b}$$

$$M_z = \frac{4\pi\Gamma}{D_{\rm kin}} \int \hat{w}^* h \left[ \partial_r \hat{w} + h' \hat{w} - \frac{h'}{\Gamma} \partial_z \hat{w} \right] {\rm d}z. \tag{C 4c}$$

In the presence of gravity the rate of change of the kinetic perturbation energy is obtained as

$$B = \frac{4\pi Gr}{ReD_{\rm kin}} \int \hat{w}^* \hat{\theta}\, r {\rm d}r\, {\rm d}z. \tag{C 5}$$

The total rate of change of energy (kinetic and thermal) is positive/negative if the growth rate of the mode is positve/negative. Hence the sign of each contribution to the energy-change rate (right-hand sides of (3.9)) determines whether a particular physical mechanism (associated with the individual term) is stabilizing or destabilizing.

Because the energy balances must be satisfied exactly, the relative numerical errors, defined as

$$\delta E_{\rm kin} := \left| \partial_t E_{\rm kin} + 1 - \sum_{i=1}^{5} I_i - M_r - M_\varphi - M_z - B \right|, \tag{C 6a}$$

$$\delta E_{\rm th} := |\partial_t E_{\rm th} + 1 - J_1 - J_2|, \tag{C 6b}$$

provide an independent check of the numerics.

## Appendix D. Volume fraction and extreme radii as functions of the contact angle

In the present numerical implementation the shape of the liquid bridge is straightforwardly parameterized by the contact angle $\alpha$. Since $\alpha$ is not easy to measure, the volume fraction $\mathscr{V}$ is usually specified in experiments. For the purpose of comparison, the volume fraction $\mathscr{V}$ and the extreme radius $h(z = 0)$ are given in figure 24 and in table 10 for zero-gravity conditions as functions of the contact angle.

## REFERENCES


Albensoeder, S., Kuhlmann, H. C. & Rath, H. J. 2000 Three-dimensional flow instabilities in the lid-driven cavity problem. *Phys. Fluids* **13**, 121.

Bayly, B. J. 1986 Three-dimensional centrifugal-type instabilities in inviscid two-dimensional flows. *Phys. Fluids* **31**, 56.

Bohm, J., Lüdge, A. & Schröder, W. 1994 Crystal growth by floating zone melting. In *Handbook of Crystal Growth* (ed. D. T. J. Hurle), Vol. 2a *Basic Techniques*, p. 213. North Holland.

Canright, D. 1994 Thermocapillary flow near a cold wall. *Phys. Fluids* **6**, 1415.

Chen, G., Lizée, A. & Roux, B. 1997 Bifurcation analysis of the thermocapillary convection in cylindrical liquid bridges. *J. Cryst. Growth* **180**, 638.

Chen, Q. S. & Hu, W. R. 1998 Influence of liquid bridge volume on instability of floating half zone convection. *Intl J. Heat Mass Transfer* **41**, 825.

Chen, Q. S., Hu, W. R. & Prasad, V. 1999 Effect of liquid bridge volume on the instability in small-Prandtl-number half zones. *J. Cryst. Growth* **203**, 261.

Drazin, P. G. & Reid, W. H. 1981 *Hydrodynamic Stability*. Cambridge University Press.

Hu, W. R., Shu, J. Z., Zhou, R. & Tang, Z. M. 1994 Influence of liquid bridge volume on the onset of oscillation in floating zone convection. *J. Cryst. Growth* **142**, 379.

Kasperski, G. & Labrosse, G. 2000 On the numerical treatment of viscous singularities in wall-confined thermocapillary convection. *Phys. Fluids* **12**, 2695.

Kelmanson, M. A. & Lonsdale, B. 1996 Eddy genesis in the double-lid-driven cavity. *Q. J. Mech. Appl. Maths* **49**, 635.

Kuhlmann, H. C. 1999 *Thermocapillary Convection in Models of Crystal Growth*. Springer tracts in modern physics, vol. 152. Springer.

Kuhlmann, H. C., Nienhüser, C. & Rath, H. J. 1999 The local flow in a wedge between a rigid wall and a surface of constant shear stress. *J. Engng Maths* **36**, 207.

Lappa, M., Savino, R. & Monti, R. 2001 Three-dimensional numerical simulation of Marangoni instabilities in non-cylindrical liquid bridges in microgravity. *Intl J. Heat Mass Transfer* **44**, 1983.

Laure, P., Roux, B. & Ben Hadid, H. 1990 Nonlinear study of the flow in a long rectangular cavity subjected to thermocapillary effect. *Phys. Fluids* A **2**, 516.

Levenstam, M. & Amberg, G. 1995 Hydrodynamic instabilities of thermocapillary flow in a half-zone. *J. Fluid Mech.* **297**, 357.

Levenstam, M., Amberg, G. & Winkler, C. 2001 Instabilities of thermocapillary convection in a half-zone at intermediate Prandtl numbers. *Phys. Fluids* **13**, 807.

Levich, V. G. & Krylov, V. S. 1969 Surface tension-driven phenomena. *Annu. Rev. Fluid Mech.* **1**, 293.

Leypoldt, J., Kuhlmann, H. C. & Rath. H. J. 2000 Three-dimensional numerical simulation of thermocapillary flows in cylindrical liquid bridges. *J. Fluid Mech.* **414**, 285.

Masud, J., Kamotani, Y. & Ostrach, S. 1997 Oscillatory thermocapillary flow in cylindrical columns of high Prandtl number fluids. *AIAA J. Thermophys. Heat Transfer* **11**, 105.

Neitzel, G. P., Chang, K.-T., Jankowski, D. F. & Mittelmann, H. D. 1993 Linear-stability theory of thermocapillary convection in a model of the float-zone crystal-growth process. *Phys. Fluids* A **5**, 108.

Neitzel, G. P., Law, C. C., Jankowski, D. F. & Mittelmann, H. D. 1991 Energy stability of thermocapillary convection in a model of the float-zone crystal-growth process. II: Nonaxisymmetric disturbances. *Phys. Fluids* A **3**, 2841.

Nepomnyashchy, A. & Simanovskii, I. 1995 Oscillatory convection instabilities in systems with an interface. *Intl J. Multiphase Flow* (*Suppl.*) **21**, 129.

Nienhüser, C., Kuhlmann, H. C., Rath, H. J. & Yoda, S. 2000 Linear stability of the two-dimensional flow in half-zones: The influence of free surface heat transfer, aspect ratio, and volume of liquid. In *Marangoni Convection Modeling Research, Anual Report, NASDA Tech. Mem.* NASDA-TMR-000006E.

Padday, J. F. 1976 Capillary forces and stability in zero-gravity environments. In *Proc. 2nd European Symp. on Materials Sciences in Space, Frascati, April 1976*, ESA-SP-114, p. 447.

Preisser, F., Schwabe, D. & Scharmann, A. 1983 Steady and oscillatory thermocapillary convection in liquid columns with free cylindrical surface. *J. Fluid Mech.* **126**, 545.

Rayleigh, Lord 1916 On the dynamics of revolving fluids. *Proc. R. Soc. Lond.* **93**, 148.

Sakurai, M. & Hirata, A. 1998 Oscillatory thermocapillary convection in a liquid bridge under normal gravity and microgravity conditions – drop shaft experiments. *Space Forum* **3**, 45.

Scriven, L. E. & Sternling, C. V. 1960 The Marangoni effects. *Nature* **187**, 186.

Shevtsova, V. S. & Legros, J. C. 1998 Oscillatory convective motion in deformed liquid bridges. *Phys. Fluids* **10**, 1621.

Smith, M. K. & Davis, S. H. 1983 Instabilities of dynamic thermocapillary liquid layers. Part 1. Convective instabilities. *J. Fluid Mech.* **132**, 119.

Sumner, L. B. S., Neitzel, G. P., Fontaine, J.-P. & Dell'Aversana, P. 2001 Oscillatory thermocapillary convection in liquid bridges with highly deformed free surfaces: Experiments and energy-stability analysis. *Phys. Fluids* **13**, 107.

Velten, R., Schwabe, D. & Scharmann, A. 1991 The periodic instability of thermocapillary convection in cylindrical liquid bridges. *Phys. Fluids* A **3**, 267.

VNI 1994 IMSL–FORTRAN *Subroutines for Mathematical Applications*. Visual Numerics Inc.

WANSCHURA, M. 1996 Lineare Instabilitäten kapillarer und natürlicher Konvektion in zylindrischen Füssigkeitsbrücken. PhD thesis, ZARM, Universität Bremen.

WANSCHURA, M., KUHLMANN, H. C. & RATH, H. J. 1997 Linear stability of two-dimensional combined buoyant-thermocapillary flow in cylindrical liquid bridges. *Phys. Rev.* E **55**, 7036.

WANSCHURA, M., SHEVTSOVA, V. S., KUHLMANN, H. C. & RATH, H. J. 1995 Convective instability mechanisms in thermocapillary liquid bridges. *Phys. Fluids* **7**, 912.